CHALMERS
UNIVERSITY OF TECHNOLOGY

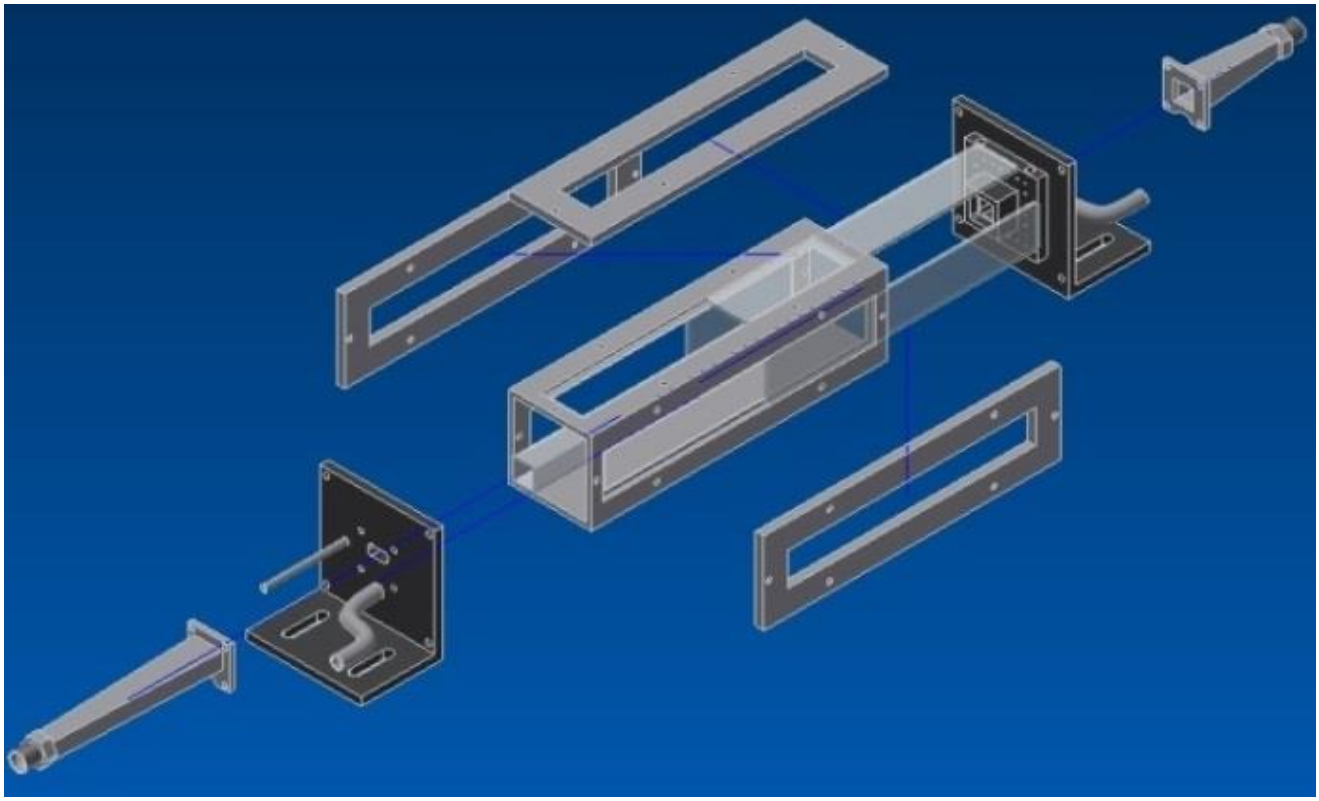

Experimental and Computational Characterization of a Novel In-Situ Reactor

Master's thesis in *Innovative and Sustainable Chemical Engineering*

PONTUS GUSTAFSON
EMIL MALMSTRÖM

Department of Applied Mechanics
CHALMERS UNIVERSITY OF TECHNOLOGY
Gothenburg, Sweden 2015

MASTER'S THESIS IN PROGRAM INNOVATIVE AND SUSTAINABLE CHEMICAL ENGINEERING (MPISC)

Experimental and Computational Characterization of a Novel In-Situ Reactor

PONTUS GUSTAFSON

EMIL MALMSTRÖM

Department of Applied Mechanics
Division of Combustion and Division of Fluid Dynamics
CHALMERS UNIVERSITY OF TECHNOLOGY
Göteborg, Sweden 2015

Experimental and Computational Characterization of a Novel In-Situ Reactor

PONTUS GUSTAFSON
EMIL MALMSTRÖM

Master's Thesis 2015:08
ISSN 1652-8557
Department of Applied Mechanics
Division of Combustion and Division of Fluid Dynamics
Chalmers University of Technology
SE-412 96 Göteborg
Sweden
Telephone: + 46 (0)31-772 1000

Cover:
CAD drawing of the In-Situ reactor. For more information, see Chapter 3.

Chalmers reproservice
Göteborg, Sweden 2015

Experimental and Computational Characterization of a Novel In-Situ Reactor
Master's thesis in Master's program Innovative and Sustainable Chemical Engineering (MPISC)
PONTUS GUSTAFSON
EMIL MALMSTRÖM
Department of Applied Mechanics
Division of Combustion and Division of Fluid Dynamics
Chalmers University of Technology

Abstract

Over the last years, the concern for environmental effects of different industrial applications has gained a great importance. One explanation for contributing to the global warming and air pollution is the release of particulate matter (PM) and carbon dioxide (CO_2) from the increasing amount of vehicles that are serving our roads. New efficient engines are under constant development to utilize the fuels in a more efficient way. This also includes the exhaust aftertreatment system (EATS) that cleans the gases from the engine exhaust.

Reducing the amount of released PM is of great importance to avoid contamination of our cities and avoid health problems such as cardiovascular diseases and lung cancer. This thesis aims to gain knowledge in the soot oxidation process to reduce release of PM to our environment.

A unique In-Situ reactor from Chalmers, designed for detailed studies of soot oxidation, has been studied both with experiments and simulations using computational fluid dynamics (CFD). An iterative method has been applied between the experiments and the simulations were the outcome from the result is trying to improve the next setup. Experiments have been performed to study the oxidation process and simulations have been executed to study the behavior of the heat and fluid flow in the reactor to improve the reactor design and the way the reactor is operated.

The results gave a good descriptions and understanding of the reactor behavior and its performance. The results include the obtained pressure drop and temperatures needed for reaction at different flow rates. As soot oxidation experiments have been executed, several conclusions have been drawn on the reaction dependencies of different temperature levels and oxidants, such as nitrogen dioxide (NO_2) and oxygen levels (O_2).

Multiphase simulations have also been performed to study the effect of thermophoresis on the deposition of particles in the reactor. The results show that the particles follow the continuous phase well and that only a small effect of thermophoresis is obtained when the reactor is used with a continuous flow of air as the heat source as in the original design. The small effect of thermophoresis indicates that particle deposit on the glass tube won't decrease the possibility to use the reactor In-Situ.

Key words: In-Situ, soot, particulate matter, Printex-U, diesel particles, EATS, oxidation, thermophoresis

Contents

Preface

This master thesis has been conducted to fulfill our Master's degree in *Innovative and Sustainable Chemical Engineering* at Chalmers University of Technology. The thesis is a cross-divisional project between the *Division of Combustion* and the *Division of Fluid Dynamics*, two divisions at the department of *Applied Mechanics*. The project therefore consisted of several different phases and involved a lot of people that we would like to acknowledge.

To our supervisors, docent Jonas Sjöblom and assistant professor Henrik Ström, we would like to address a special thank you. Without your ideas, which was the startup of this project with a unique prototype designed reactor, this thesis would never have been written. Without your constant support and knowledge within respectively field, we would not have made it. We would also like to address our gratitude to all people involved in the lab and workshop at *Division of Combustion* for their assisting in practical problems and the modifications that arises when working with prototype designs.

The experimental part was carried out at *Competence Center for Catalysis (KCK), Chalmers.* We therefore would like to thank PhD student Mattias Englund for letting us join and use his laboratory as well for assisting during the experimental part.

At last, we would like to thank our examiners, professor Sven B Andersson and professor Srdjan Sasic as well as our family and friends who stood us by this entire project when we needed it the most.

Göteborg June 2015-06-04

PONTUS GUSTAFSON
EMIL MALMSTRÖM

List of abbreviations

Ar	Argon
CFD	Computational fluid dynamics
CO	Carbon monoxide
CO_2	Carbon dioxide
DPF	Diesel particulate filter
DOC	Diesel oxidation catalyst
EATS	Exhaust aftertreatment system
HC	Hydrocarbons
H_2O	Water
Kn	Knudsen number
NO	Nitrogen oxide
NO_2	Nitrogen dioxide
NO_x	Nitrogen oxides (NO and NO_2)
O_2	Oxygen
PM	Particulate matter
SCR	Selective catalytic reduction
SO_2	Sulfur dioxide
UDF	User defined function

Nomenclature

A	Pre exponential factor	[-]
A_{cross}	Cross sectional area of particle	[m^2]
Airflow	Referring to distributed air from small holes	
Air inlet	Referring to air inlet with counter current flow	
Air outlet	Referring to air outlet with counter current flow	
α	Conversion	[-]
C	Speed of sound	[m/s]
C_c	Cunningham correction factor	[-]
C_D	Drag coefficient	[-]
D_p	Particle diameter	[m]
D_T	Thermophoretic coefficient	[-]
E	Energy	[Joule]
E_A	Activation energy	[kJ/mole]
F_D	Drag force	[kg·m/s^2]
F_B	Brownian motion	[kg·m/s^2]
F_{Bouy}	Buoyancy force	[kg·m/s^2]
F_T	Thermophoretic force	[kg·m/s^2]
ϕ	Velocity fraction	[-]
Gasflow	Referring to gas mixture containing oxidants	[-]
g_i	Acceleration due to gravity	[m/s^2]
γ	Selectivity	[-]
y_i	Height over reference	[m]
Kn	Knudsen number	[-]
λ	Mean free path	[m]
μ_c	Viscosity of continuous phase	[Pas]
m_0	Initial mass of soot	[kg]
m_p	Mass of particles	[kg]
M	Mach number	[-]
n_f	Number of injected particles per time step	[#/s]
n_{max}	Maximum number of parcels in reactor	[#]
P	Pressure	[Pascal]
Δp_f	Pressure losses	[Pascal]
ρ_c	Density of continuous phase	[kg/m^3]
ρ_d	Density of particles	[kg/m^3]
R	Gas constant	[J/mole·K]
Re	Reynolds number	[-]
Re_p	Particle Reynolds number	[-]
St	Stokes number	[-]
τ	Residence time	[s]
τ_{xp}	Particle response time	[s]
τ_f	Characteristic time scale of the flow	[s]
Δt	Time step	[s]
u_i	Velocity	[m/s]
u_c-u_d	Slip velocity	[m/s]
V_P	Volume of particle	[m^3]

1 Introduction

1.1 Background

The effect of global warming due to release of greenhouse gases, such as carbon dioxide (CO_2), and health problems due to air pollution of particulate matter (PM) have been severe the last years. This can be noticed both in climate change and for instance in increase of cardiovascular diseases [1]. Nevertheless, more heavy transport is driving on our highways and the amount of passenger cars is still increasing [2]. As long as the automotive industry produces vehicles that run by liquid fuels, emissions will always be an issue and cleaning of exhaust gases will be of utmost importance.

Diesel engines produce a mixture of several different components that are released with the exhaust gases, either in form of gaseous compounds or solid particles. Common components include carbon dioxide, carbon monoxide, nitrogen oxides and a large variety of hydrocarbons [3]. The particles, known as particulate matter, can have various composition and are very small, typically a particle diameter of $< 2.5\mu m$ with a subgroup including ultrafine particles with diameter $< 0.1\mu m$ [3].

In order to reduce the amount of particulate matter a diesel particle filter (DPF) is commonly used, which significantly can reduce the amount of particles in the exhaust gas. Problems might however occur when implementing lab scale (experiments) results at full-scale production (DPF in diesel vehicle). In order to facilitate this transition, CFD simulations together with experiments can be a good tool to scale-up a model from lab scale and predict the behavior at commonly used DPF from industry.

Using an In-Situ reactor with visual access would give the possibility to actually look at the oxidation, study effects of thermophoresis and monitor the heat front during combustion.

1.2 Objectives of the thesis

The aim of this master thesis is to characterize an In-Situ reactor designed at Chalmers for particle oxidation. This will be done by performing experiments with synthetic soot in the form of Printex-U, which will be heated to an appropriate temperature. The experiments will include different oxidants and concentrations to be able to discuss how, and what parameters that are affecting the oxidation process.

Together with the experimental part, computational fluid dynamics (CFD) simulations will be performed to characterize the reactor. The CFD simulations will generate results of which operating conditions that are needed for the reactor to work satisfactory and oxidation to occur. The objectives of this thesis are:

- To characterize the reactor in detail by studying the flow field, pressure drops and the temperature field with possible temperature gradients. Insulation of the reactor and measurements of temperatures and pressure drops with experiments will be performed that will be confirmed by CFD simulations.

- To implement a soot oxidation model into the CFD software ANSYS FLUENT and to perform preloaded soot oxidation simulations with synthetic soot (Printex-U) and a mixture of nitrogen dioxide, oxygen and argon as the carrier gas.
- To predict the capture efficiency of dispersed soot particles, including the effects due to the presence of thermophoresis, via CFD simulations.

1.3 Organization of the thesis

This thesis is first presenting a theoretical background of the processes to clean the diesel engine exhaust and the commonly used equipment to perform these operations. The theory chapter also includes important phenomena for simulating multiphase flows as well as a basic background in computational fluid dynamics (CFD). The performed experiments and simulations are presented in two separate chapters while the result is presented and analyzed together.

The thesis is finalized with a discussion of the work and some comments of the importance to continue this work and other activities within this research area in the future.

1.4 Methodology

The intention with this project is to be an iterative project, performing both simulations and experiments. The result and outcome of the project will give better understanding of the soot oxidation and the designed In-Situ reactor. The iterative process can be found in Figure 1-1 with a cross reference to each individual result.

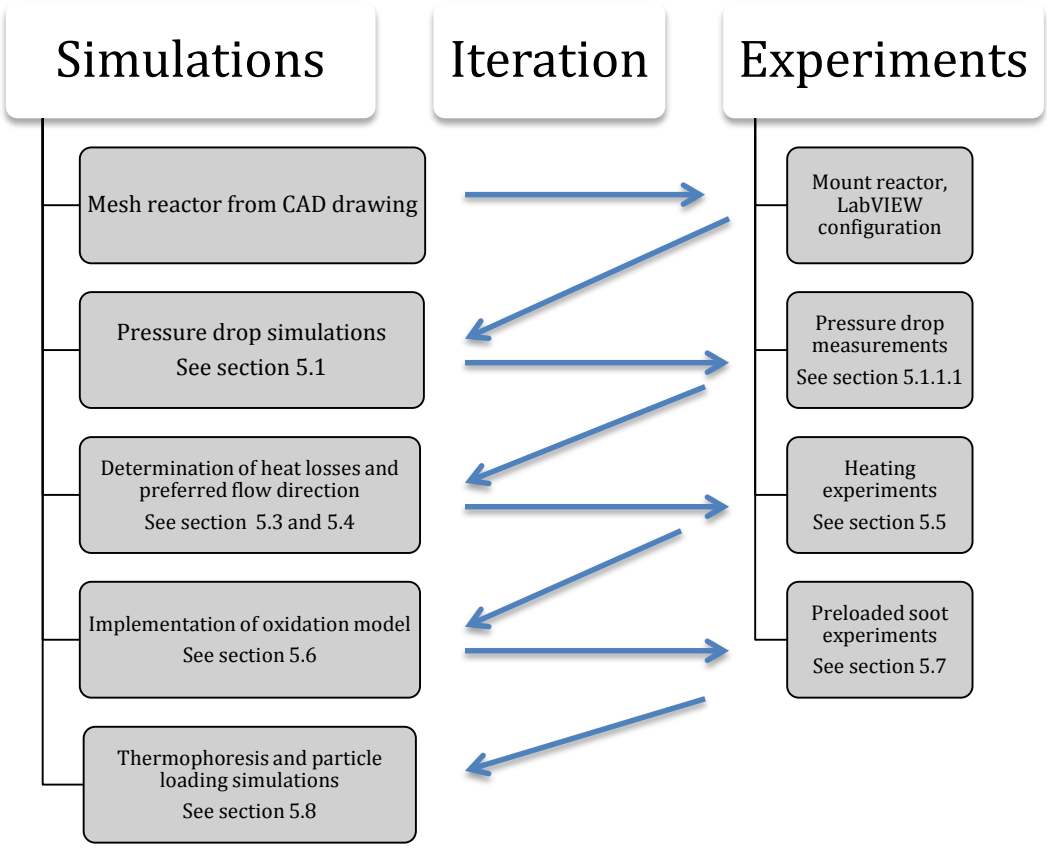

Figure 1-1 Iterative process through the project.

2 Theory

2.1 Particulate matter

Particulate matter (PM) consists of several components in different mixtures, both organic and inorganic substances [1]. The chemical composition of the particulate matter will vary and depends on factors like engine type, fuel compositions and commonly consist of about 75% elemental carbon, 19% organics compounds and the rest inorganic compounds [3]. Inorganic compounds typically originate from wear, traces of lubricant oil and ash from combustion.

Figure 2-1 is showing the size distribution of typical particulate matter. The solid line represents the number distribution while the dotted line represents the mass distribution and the y-axis is a normalized concentration. It is clearly seen that the major amount of particulate matter have a diameter below 50 nm while the mass distribution peaks at clearly larger particles in the so called *accumulation mode,* see Figure 2-1 [4].

The greatest amount of the particulate matter exists in the so called *nuclei mode* region. These particles primarily consist of elemental carbon and are produced already in the engine due to combustion [3]. Due to several mechanisms occurring in the exhaust aftertreatment system they will increase in amount. Mechanisms such as cooling and condensation will form particles of hydrocarbons and ash as well.

The larger particles found in the *accumulation mode* are typically formed from several smaller particles as well as from combustion. Due to the nanometer size, the surface area per volume is large which will tend to attract other particles and cause agglomeration [3]. Accumulation mode particles can also be formed due to condensation of sulfur compounds or hydrocarbons onto a carbon nuclei or ash particle, which will increase the particle diameter [3, 4]. A schematic figure of the *accumulation mode* particles are shown in Figure 2-2.

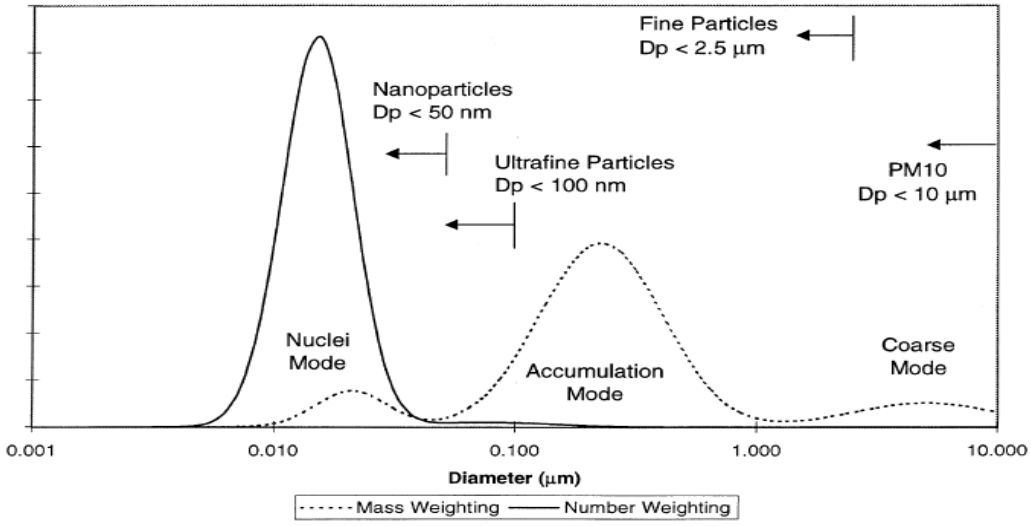

Figure 2-1 Size distribution of particulate matter [4].

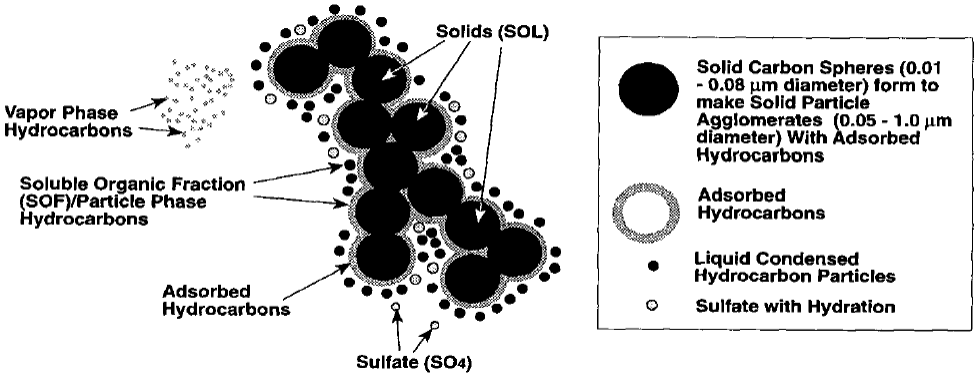

Figure 2-2 Diesel particles and vapor phase compounds [5].

The *coarse mode* particles in Figure 2-1 are very small at a number distribution while the mass distribution is in the order of magnitude as the *nuclei mode*. These particles consist of *accumulation mode* particles that have been deposited on the exhaust aftertreatment system and later on re-entrained [4].

2.1.1 Health aspects of particulate matter

Even though the ambient air concentration of particulate matter has decreased the last years due to efficient development of new exhaust aftertreatment systems, the levels present are still a health hazard [1, 6]. The concentration of particulate matter in air is not just a health risk but also contaminates the environment, decreases visibility, contributes to soiling of buildings as well as to increase of engine wear and fouling of aftertreatment systems [4].

Several studies assess the smallest particles, *nuclei mode*, to be the most harmful [4]. Health hazards have been noticed both at short exposure and long term. Short term exposure of particulate matter can lead to dizziness and irritations of throat and eyes while long term exposure can have fatal consequences by respiratory diseases, reduced lung function and even lung cancer [1, 3].

The major problem with the particulate matter and the reason for high health risks are the size. With a particle diameter of nanometer size, the particles have good possibilities to penetrate and be transported by our respiratory system [7]. In 2013, an estimate of 2.1 million people worldwide died due to air pollution of PM [8].

2.2 Diesel engines

Diesel engines are widely used in several different areas such as automotive industry, trains, boats, industrial applications and many more.

The diesel engine is categorized as a compression-ignition engine. This means that no external ignition source is needed for combustion. Primary air is compressed into the combustion chamber and when desired pressure and temperature is reached, an injection of diesel to the combustion chamber will cause self-ignition of the system.

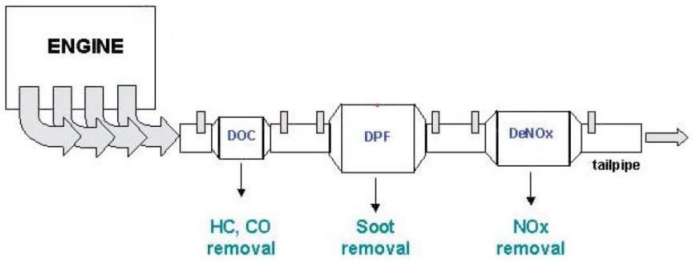

Figure 2-3 Schematic view of exhaust after treatment system [9].

Diesel engines are much more effective than gasoline engines in combustion of hydrocarbons and almost no carbon monoxide is released. This due to the operating condition of high air-to-fuel ratio. Other benefits of the diesel engine are lower emissions at cold-start and almost zero emissions from evaporation during fuelling due to lower volatility of diesel than gasoline [10].

The major challenge for the diesel engine is to reduce the release of particulate matter, nitrogen monoxide (NO) and nitrogen dioxide (NO_2) [10].

2.2.1 Exhaust aftertreatment system (EATS)

For efficient removal of emissions, the aftertreatment system consists of several components and separation stages. A schematic view of the different separation stages is shown in Figure 2-3.

2.2.1.1 DOC

The DOC, diesel oxidation catalyst, is a monolith reactor that is used to oxidize gaseous pollutants. Leftovers from incomplete combustion like carbon monoxide (CO) and different kinds of hydrocarbons (HC) are converted into carbon dioxide (CO_2) and water (H_2O) [11]. However, the catalyst is not selective for just hydrocarbons and will oxidize other compounds as well. This might lead to an increase of particulate matter when for instance sulfur dioxide (SO_2) is oxidized and, as a consequence, sulfate particles are created [12]. This is however a minor issue since the sulfur level in modern fuels is very low.

Oxidation of nitrogen compounds in the DOC will have a positive effect on the soot oxidation process since the reduction of particulate matter can be performed at lower temperature with NO_2 compared to NO in the following separation stage, the diesel particulate filter [13].

2.2.1.2 DPF

The most common way to reduce particulate matter in diesel applications is to use a diesel particulate filter (DPF) [11]. The DPF consist of a monolith reactor but with one side of every channel being plugged i.e. every channel is open in one end and closed in the other. This design will force the exhaust gas to flow through the porous walls while the solid particles will deposit in the channels and pores, see Figure 2-4.

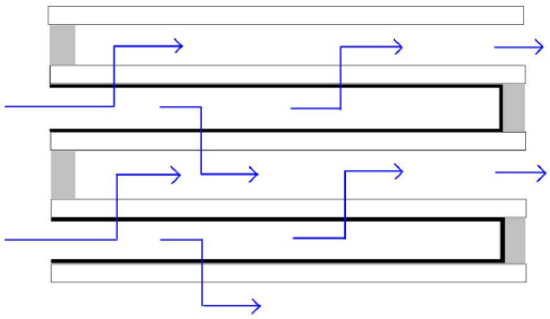

Figure 2-4 Schematic figure of DPF, a monolith with one plugged end of every channel [11].

This configuration reaches a capture efficiency of over 90% but with the drawback of an increased pressure drop [14].

Figure 2-4 is showing a schematic description of a commonly used DPF design. One end of every channel being plugged and one open. At the right hand side of the figure, clean exhaust gas is leaving the system while particulate matter will deposit in the channels and as a consequence, very few solid particles will leave the DPF.

2.2.1.3 DeNO$_x$

The last component of the exhaust aftertreatment system will reduce the nitrogen dioxides (NO_x) concentration released to ambient air. There are several possible techniques but the most common is to use a selective catalytic reduction (SCR) catalyst, which is commonly used with ammonia (NH_3) as the reducing agent [15].

2.3 Heat and fluid flow

2.3.1 Concept of continuum

Liquids and gases are commonly referred to as fluids. When properties like velocity and densities of fluids vary continuously from one point to another a fluid can be considered to consisting of continuous matter, i.e. continuum. Since fluids are consisting of a huge amount of molecules, it is not reasonable to predict the motion of every single one of them. For instance, one cubic centimeter of atmospheric air contains $2.5 \cdot 10^{19}$ molecules [16]. Considering an infinitely small control volume, the density of a fluid will change as the control volume is increased if not containing more molecules. However, if the control volume contains enough molecules, a statistical average can be obtained and a proper density can be defined. Thereby, the continuum assumption can be justified for fluids [17].

2.3.1.1 Rarefied flows

A possible way to judge whether the continuum concept is valid is to analyze the Knudsen number (Kn). The Knudsen number is defined as Equation (2-1).

$$\boldsymbol{Kn} = \frac{\boldsymbol{\lambda}}{\boldsymbol{L}} \qquad \textbf{(2-1)}$$

Where λ is the mean free path of the gas and L a characteristic length [18]. In order for the continuum concept to be valid, the Knudsen number must be less than 10^{-3} [17]. For air at atmospheric pressure the mean free path is approximately 67 nm [11] and can be calculated according to Equation (2-2) [19].

$$\boldsymbol{\lambda = \frac{\mu_c}{0.499 \cdot \rho_c \cdot \sqrt{\frac{8 \cdot P}{\pi \cdot \rho_c}}}} \qquad \textbf{(2-2)}$$

Where μ_c is the viscosity of the gas, ρ_c the density of the gas and P is the pressure.

2.3.2 Navier-Stokes equations

The Navier-Stokes equations were derived under assumption of fluids being regarded as continuum [17]. The Navier-Stokes equations are limited to macroscopic conditions and were derived from two fundamental principles: the conservation of mass and Newton's second law of motion [20]. The principle of conservation of mass is commonly referred to as the continuity equation and for an incompressible fluid, written in differential form, it reads as Equation (2-3):

$$\boldsymbol{\frac{\partial u_i}{\partial x_i} = 0} \qquad \textbf{(2-3)}$$

The law simply states that mass cannot be created nor destroyed and that the rate of mass accumulation plus the net efflux of mass equals zero [17].

Newton's second law of motion states that the force on a fluid in a control volume equals the sum of the momentum accumulation in that control volume and the net efflux of momentum from the control volume. The equations derived from Newton's second law in three dimensions are known as the Navier-Stokes equations and is in Equation (2-4) written in differential form [11, 21].

$$\boldsymbol{\rho\left(\frac{\partial u_i}{\partial t} + u_j \frac{\partial u_i}{\partial x_j}\right) = -\frac{\partial p}{\partial x_i} + \frac{\partial}{\partial x_j}\left(\mu \frac{\partial u_i}{\partial x_j}\right) + \rho \cdot g_i} \qquad \textbf{(2-4)}$$

The solution of these equations will yield a pressure- and velocity field, which gives information of the spatial and temporal variation of a fluid flow in a given system.

2.3.3 Energy transport

Solving the energy equation in a fluid flow also requires a transport equation. Energy can be divided into several subgroups such as kinetic energy, thermal energy and potential energy. The equation used and solved by *Fluent* for total energy is shown in Equation (2-5).

$$\frac{\partial E}{\partial t} = -\frac{\partial}{\partial x_j}\left[EU_j - k_{eff}\frac{\partial T}{\partial x_i} - \tau_{kj}U_k\right] + S_E \qquad \textbf{(2-5)}$$

Where the terms from left to right are accumulation of energy, transport of energy due to convection, conductivity, viscous dissipation and a source term, typical heat from a chemical reaction.

2.3.4 Computational Fluid Dynamics (CFD)

Solving the Navier-Stokes equations is extremely computationally heavy for flow involving high Reynolds numbers and only possible for the simplest of problems. The reason for this is due to the second term on the left-hand side of Equation (2-4), which makes the equations a non-linear partial differential equation system. This requires the solution to be obtained numerically instead of analytically, a procedure that is possible with computational fluid dynamics (CFD).

To enable a solution with CFD the entire domain of interest is divided into small sub volumes, i.e. cells. At these discretized cells, the governing equations can be reformulated as a set of linear algebraic equations and solved in an iterative manner [18].

2.3.5 Important parameters for analyzing multiphase flows

In order to analyze multiphase flows, several different dimensionless numbers can be used. To most common is the Stokes number (St) and particle Reynolds number (Re_p). The Stokes number is a ratio between the particle response time (τ_{xp}) and characteristic time scale of the fluid (τ_f). The Stokes number gives information about how the particle will follow or behave in the fluid and whether it follow the streamlines. According to the ratio, conclusion can be drawn that for low Stokes number (St<<1), the particle will follow the streamlines associated with the fluid well since the response time of the particle is very short comparing to the one of the fluid. At high Stokes numbers, the scenario is the opposite; it takes a long time for the particle to react to a change. The Stokes number is defined by Equation (2-6).

$$\boldsymbol{St = \frac{\tau_{xp}}{\tau_f}} \qquad \textbf{(2-6)}$$

The particle response time is by definition the time required for a particle released from rest to achieve 63% of the free stream velocity [17]. The particle response time is defined by Equation (2-7):

$$\boldsymbol{\tau_{xp} = \frac{\rho_d \cdot D_p^2}{18 \cdot \mu_c} \cdot \frac{24}{C_D \cdot Re_p}} \qquad \textbf{(2-7)}$$

where ρ_d is the density of the particle, D_p the particle diameter, μ_c the viscosity of the carrying phase, C_D the drag coefficient and Re_p the particle Reynolds number. If Re_p<<1, the flow is said to be in the *Stokes regime* or *Stokes flow* and the factor $24/C_D \cdot Re_p$ in Equation (2-7) approaches unity for flows when the continuum assumption is verified [17].

$$\boldsymbol{Re_p = \frac{\rho_c \cdot D_p |u_c - u_d|}{\mu_c}} \qquad \textbf{(2-8)}$$

The particle Reynolds number is defined by Equation (2-8). Where ρ_c is the density of the carrying phase, D_p the particle diameter, μ_c the viscosity of the carrying phase, u_c the velocity of the carrying phase and u_d the velocity of the particle.

2.3.6 Motion of a particle

To derive the equation of motion of a particle dispersed in a fluid, Newton's second law of motion is being applied. By integrating over the entire particle surface and evaluate the pressure- and viscous forces as well as the body forces, the motion can be decided as the net action of these forces [22].

$$\boldsymbol{m_p \frac{du_{p,i}}{dt} = m_p \cdot g_i + \oint_s \left[-p \cdot \delta_{ij} + \mu \left(\frac{\partial u_i}{\partial x_j} + \frac{\partial u_j}{\partial x_i} \right) \right] n_j dS} \qquad \textbf{(2-9)}$$

To solve Equation (2-9) the exact motion of the fluid around the particle need to be resolved which is only possibly for a few numbers of particles and today not possible for common industrial applications. Instead, Equation (2-9) needs to be modeled. This is done by summation of forces (ΣF_i) according to Equation (2-10) where every force considered affecting the solution would be added, using the averaged properties for the fluid in that computational cell. The forces applied and considered in this thesis will be further explained in the following sections.

$$\boldsymbol{m_p \frac{du_{p,i}}{dt} = \sum F_i} \qquad \textbf{(2-10)}$$

2.3.6.1 Drag force

The drag force (F_D) is commonly the most important force for particle-fluid interaction. The drag force arises when a particle is being exposed to a velocity field and acts opposite to the relative motion of the particle [23]. The drag force is expressed in Equation (2-11):

$$\boldsymbol{F_D = \frac{1}{2} \rho_c \cdot C_D \cdot A_{cross} |u_c - u_p| (u_c - u_p)} \qquad \textbf{(2-11)}$$

u_c-u_p is known as the relative velocity between the continuous phase and the particle or commonly the *slip velocity* [17]. A_{cross} is the cross sectional area of the particle, ρ_c the density of the continuous phase while C_D is the drag coefficient. For Stokes flow ($Re_p << 1$), the drag force can be calculated directly (provided the continuum concept is valid) but for larger Reynolds numbers, the drag force must be modeled through C_D.

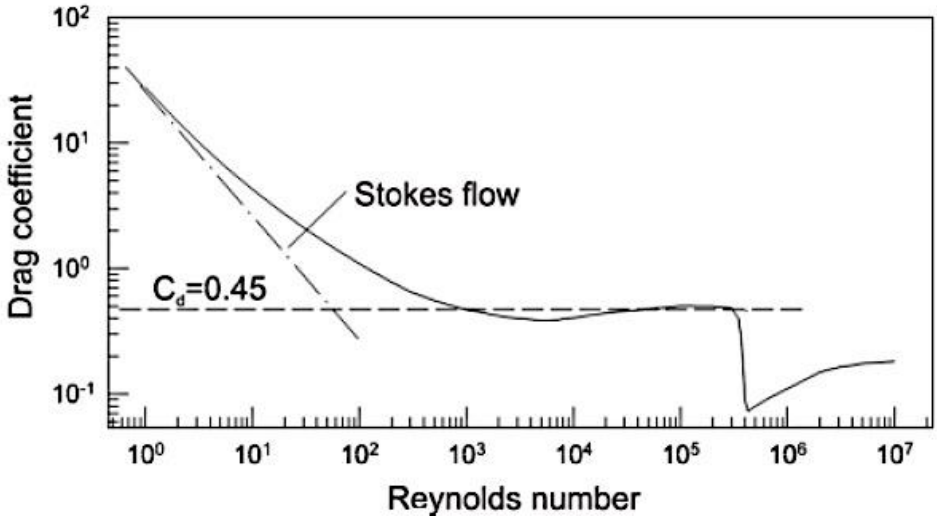

Figure 2-5 Standard drag curve, drag coefficient as a function of Reynolds number [17].

The drag coefficient is a function of several parameters such as particle shape, Mach number and Reynolds number [24]. For the simplest of cases, a non-rotating sphere, the drag coefficient is only a function of the Reynolds number and can be estimated from Figure 2-5, this is commonly known as the *standard drag curve* [17, 18].

2.3.6.2 Buoyancy force

The buoyancy force ($F_{i,Buoy}$) or gravity force originates from Archimedes' principle that simply states that the buoyancy force exerted on an object equals the weight of the fluid that the body displaces. The force acts opposite the direction of gravity and is expressed in Equation (2-12) [25].

$$\boldsymbol{F_{i,Buoy} = (\rho_p - \rho_c) \cdot V_p \cdot g_i} \qquad \textbf{(2-12)}$$

Where ρ_c is the density of the continuous phase, ρ_d is the density of the particle, V_p the volume of the particle and g_i the gravity. Buoyancy force is categorized as a body force and is the most common one. Other body forces include Coulomb forces, which are only affecting a system exposed to an electric field and the thermophoretic force [17].

2.3.6.3 Thermophoretic force

In a dispersed gas-solids system of nanoparticles, a thermophoretic force arises from a temperature gradient in the continuous phase and imposes a net force on the particles in the direction of decreasing temperature [26]. The motion of a particle due to this force is called *thermophoresis*, but the phenomenon only affects submicron particles [18, 27]. The force is given by Equation (2-13).

$$F_T = -D_T \cdot \frac{1}{T} \nabla T \qquad \textbf{(2-13)}$$

where D_T is the thermophoretic coefficient, T the temperature and ∇T the temperature gradient.

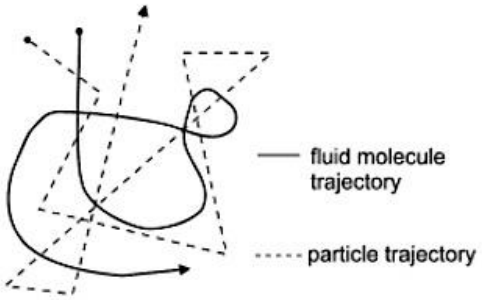

Figure 2-6 Particle motion due to Brownian motion [17].

2.3.6.4 Brownian motion

For small particles (particle diameter <1μm), Brownian motion is significant. Brownian motion is a diffusion process which is arises due collisions between particles and molecules and is thereby a random motion. Particles either suspended in gases or liquids are affected by Brownian motion but the fluctuations will be higher with a gas as the carrying phase [17]. The force due to Brownian motion is expressed in Equation (2-14).

$$F_B = m_p \cdot \zeta_i \sqrt{\frac{\pi \cdot S_0}{\Delta t}} \tag{2-14}$$

Where ζ_I is a random number and S_0 is a function of the particle diameter and density, temperature and the Cunningham correction factor.

2.4 Pressure drop

To describe a system properly, pressure is often of great importance. When designing new reactors or other mechanical equipment, considerations must always be taken to the pressure so the equipment can withstand the pressure it is being exposed to. Pressure can both be applied to a system statically and be built up inside a volume due to pressure drop from a fluid flow.

The most commonly and applied way to describe pressure drop is by the Bernoulli equation described in Equation (2-15) [23].

$$g \cdot y_1 + \frac{v_1^2}{2} + \frac{P_1}{\rho} = g \cdot y_2 + \frac{v_2^2}{2} + \frac{P_2}{\rho} \tag{2-15}$$

Where y_i is the height, v_i the velocity, P_i the pressure, g the gravitational constant and ρ the density of the fluid.

The equation were developed during the assumptions of inviscid- and steady flow, incompressible flow with no heat transfer or work being applied to the system.
If friction and losses is taken into considerations, Equation (2-15) is extended according to Equation (2-16) [28].

$$g \cdot y_1 + \frac{v_1^2}{2} + \frac{P_1}{\rho} = g \cdot y_2 + \frac{v_2^2}{2} + \frac{P_2}{\rho} + \Delta p_f \quad \textbf{(2-16)}$$

Where Δp_f is the pressure drop or loss between point 1 and 2. The factor Δp_f is a function of length and diameter of the pipe, Reynolds number, as well as the friction factor of the pipe material and velocity. As Δp_f is increasing with increased velocity, a larger volumetric flow will generate a larger pressure drop [28].

In addition to this, there will always be losses in pipe openings, which can be described by a coefficient of discharge. This coefficient will always be less than unity and thereby giving an outlet velocity lower than calculated with the Bernoulli equation for an ideal case [28]. If a fluid flow from a pipe is entering the ambient air, the pressure is always atmospheric. This means that the pressure drop will be the built up, overpressure, in the interior volume.

2.4.1 Mach number

Mach number (*M*) is a dimensionless number, describing the ratio of a fluid velocity and the speed of sound according to Equation (2-17) [23].

$$M = \frac{v}{C} \quad \textbf{(2-17)}$$

Where *v* is the fluid velocity and *C* the speed of sound. Parameters that are affecting the value of speed of sound are temperature and pressure [28].

Liquids are normally treated as incompressible while gaseous compounds are compressible. Whether compressible effects are of importance is often judged by analyzing the Mach number. As a rule of thumb, gases can be treated as incompressible when M<0.2-0.3 with a negligible calculation error [23]. Effects that do occur at larger Mach numbers consist of formation of shockwaves, density increase of the gas and larger drag coefficient [17].

2.5 Kinetic models

This chapter describes the chemical reactions occurring in the oxidation process of soot. When simulating the reactions, soot is considered to solely consist of carbon (C).

2.5.1 Oxidation with NO_2

The overall reaction formula used to describe the soot oxidation can be seen in Equation (2-18) [29].

$$\boldsymbol{C + (2-\gamma)NO_2 \rightarrow \gamma CO + (1-\gamma)CO_2 + (2-\gamma)NO} \quad \textbf{(2-18)}$$

Carbon (C), represents the synthetic soot and γ represents the selectivity towards different products, which will vary with temperature and is increased with increased temperature.

$$\boldsymbol{k = A \cdot e^{\left[-\frac{E_a}{R}\left(\frac{1}{T}-\frac{1}{T_{ref}}\right)\right]}} \quad \textbf{(2-19)}$$

By using the Arrhenius expression in Equation (2-19) where A is a pre-exponential factor, E_a the activation energy and R the gas constant, the final rate expression becomes (2-20):

$$\boldsymbol{r = k \cdot f(\alpha) \cdot \left(P_{NO_2} \cdot 1000\right)^{\beta} \cdot m_o} \quad \textbf{(2-20)}$$

Where $f(\alpha)$ is calculated as Equation (2-21) and α is the conversion, k the rate constant, P_{NO2} the partial pressure of NO_2 and m_0 the initial mass of soot. Thereby the product $f(\alpha) \cdot m_0$ becomes the remaining mass soot on the monolith layer.

$$\boldsymbol{f(\alpha) = 1 - \alpha} \quad \textbf{(2-21)}$$

2.5.2 Oxidation with NO_2 + O_2

Performing oxidation with both nitrogen dioxide and oxygen will add a second reaction, which will occur in parallel with Equation (2-18).

$$\boldsymbol{C + (1 - 0.5\gamma)O_2 \rightarrow \gamma CO + (1-\gamma)CO_2} \quad \textbf{(2-22)}$$

Using Equation (2-18) and (2-22) combined, the rate expression will be updated according to Equation (2-23) [29].

$$\boldsymbol{r = k \cdot f(\alpha) \cdot \left(P_{O_2} \cdot 100\right)^{\beta} \cdot \left(P_{NO_2} \cdot 1000\right)^{\beta} \cdot m_o} \quad \textbf{(2-23)}$$

Data of constants are found in Appendices D. As the products from Equation (2-23) exist in Equation (2-18), there is however impossible to judge whether the oxidized carbon is reacting with oxygen (O_2) or NO_2.

2.5.3 Thermodynamic equilibrium

The presence of oxygen in the gas mixture has one other positive effect in the oxidation process except than oxidizing the soot. The activation energy of the mixture is lower than with pure NO_2, which enhances oxidation at lower temperatures. The mixture has previously shown formation of CO_2 below 400°C while pure NO_2 and pure O_2 start to oxidize soot just above 400°C and 550°C respectively [29].

One explanation for this is that NO_2 is naturally decomposing to NO according to Equation (2-24) [30].

$$2NO_2 \leftrightarrow 2NO + O_2 \quad \textbf{(2-24)}$$

The equilibrium is determined by the concentration of oxygen, large amount of oxygen generating large amount of NO_2. This means that oxygen is stabilizing the NO_2 and thereby more NO_2 is available for oxidation. The thermodynamic equilibrium is dependent on temperature as shown in Figure 2-7 and calculated by properties such as entropy and enthalpy.

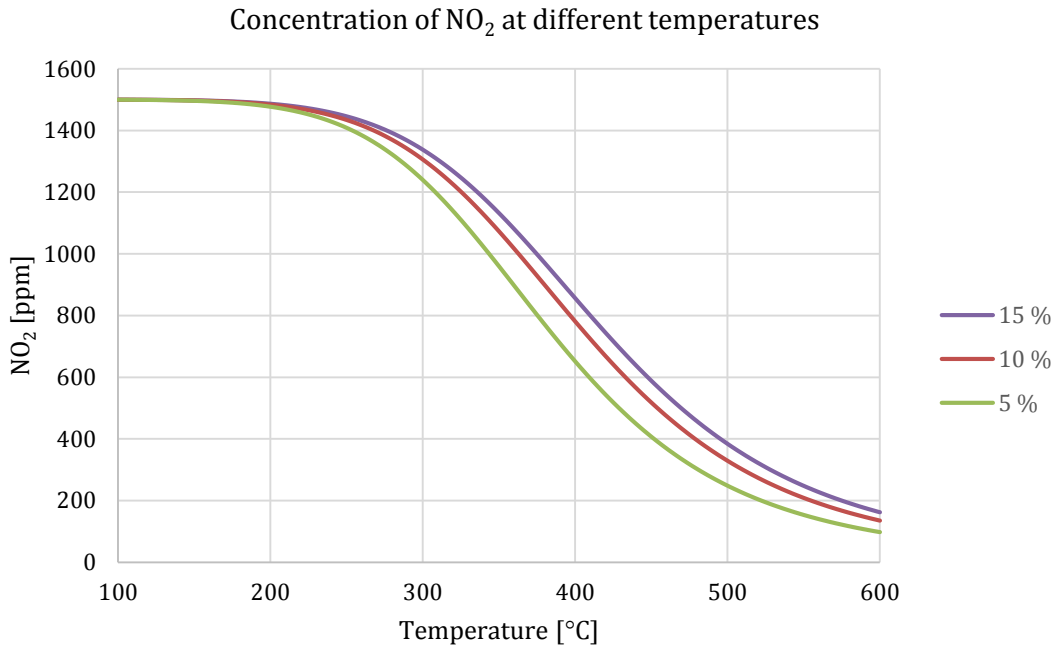

Figure 2-7 Concentration of NO_2 at different temperatures with different concentrations of O_2 (5%, 10% and 15%).

3 Experiments

3.1 Reactor design

The reactor used for both experiments and simulations is designed and constructed according to Figure 3-1.

As can be seen from Figure 3-1 the reactor will have three possible In-Situ options, one on each side and one on the top where combustion of Printex-U can easily be observed. The construction consists of stainless steel and quartz glass with high thermal resistance that will be needed at high operating temperature (>400°C). There is one inlet and one outlet where the exhaust gas will flow and, outside of this section, the reactor will be isolated by a flow of hot air. On each side there will also be possibilities to measure temperature by inserting a thermocouple.

Figure 3-2 is showing the in- and outside of the rear part of the reactor. The straight pipe is to be used as the entrance of a thermocouple and the bent pipe for inlet flow of hot air as insulation. As the air enters the outer part of the reactor volume it is spread by 24 holes to obtain an even distribution of air throughout the reactor volume. Maintaining constant temperature is very critical during experiments with chemical reactions since chemical kinetics are highly dependent on temperature [31]. The exhaust gas will flow in a inner glass pipe placed in the center between the two ends, see Figure 3-3.

The length of the glass pipe for the gas flow is 152.4 mm (6 inch) with an inside width and height of 12 mm. The cross sectional area available for airflow is 1740 mm^2. The diameter of the 24 air holes is 0.75 mm at the inlet while they are 0.5 mm at the outlet, provided that the air is flowing counter current.

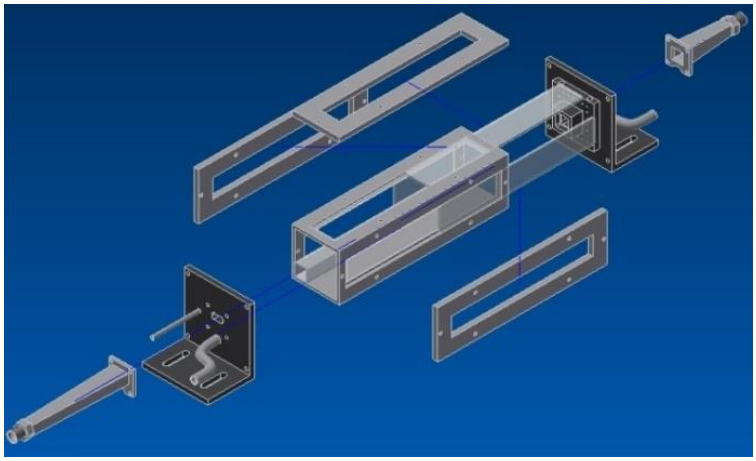

Figure 3-1 CAD drawing of the reactor.

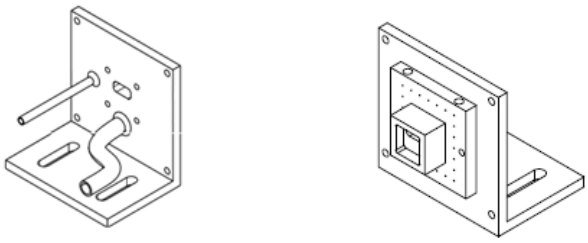

Figure 3-2 One side of the reactor, holes can be seen for air distribution.

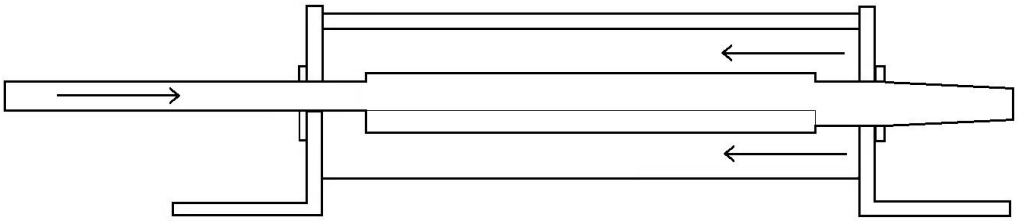

Figure 3-3 Cross section of the reactor. Arrow pointing right shows the gas flow while the two arrows pointing left describes the airflow. The top layer of the monolith can be seen in the middle of the reactor as a grey line.

As can be seen from Figure 3-2, the air enters at the bend pipe (left) and is spread by 24 holes of smaller diameter (right). For results of pressure drop calculations, air inlet and outlet is referring to Figure 3-2 with different diameters.

3.2 Experimental set-up

Experiments were performed to study the oxidation of synthetic soot. The formation of CO_2 was monitored by a mass spectrometer, which distinguishes molecules by their molecular weight. The exhaust gas was fed to the mass spectrometer from the reactor with argon (Ar) as inert gas. By calibrating the spectrometer with known concentrations of CO_2, the oxidation of soot can be studied by analyzing the concentration of CO_2 leaving the system.

Printex-U was applied onto the monolith as Figure 3-5a. An estimated mass of 1 mg soot was applied but with poor scale accuracy at these low weights, the exact amount of soot is only known by integrating the amount of carbon leaving the reactor system. It is therefore important to achieve a complete combustion of the applied Printex-U.

Four thermocouples were used at different positions in the monolith channels for monitoring the temperatures during experiment according to Figure 3-4. In addition to this, the temperature was measured outside the reactor to not exceed the temperature specification of the heat tape as well as the gas inlet temperature that controlled the regulator of the heat tape. Between the reactor exhaust and the spectrometer, a filter was applied to separate unburned particles from the spectrometer.

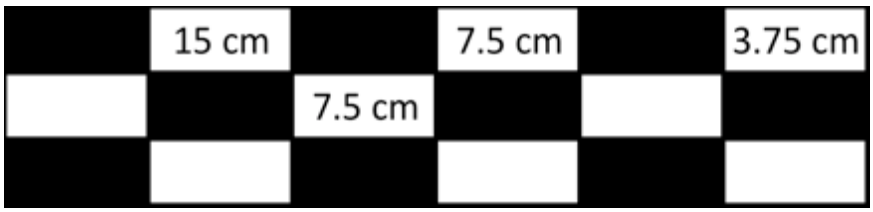

Figure 3-4 Position of the four thermocouples in the monolith channels. The length refers to how far the thermocouples are placed in the monolith.

Before an experiment was conducted, heat tape was also applied to the reactor volume and the complete setup was isolated with glass wool and aluminum foil according to Figure 3-6b. While heating the reactor to a proper temperature, a flow of argon through the reactor was applied to ensure zero concentration of air in the reactor.

The experiment was performed at a constant temperature of 430°C and a total volumetric flow of 330 ml/min. Several different concentrations of oxidants levels were investigated during one long consecutive run. These were as follows:

- 1500 ppm NO_2
- 1500 ppm NO_2 and 10 % O_2
- 1500 ppm NO_2 and 15 % O_2
- 1500 ppm NO_2 and 5 % O_2
- 2000 ppm NO_2 and 5 % O_2
- 1000 ppm NO_2 and 5 % O_2

The flow of gas species and inert gas of argon were all controlled by mass flow controllers from Bronkhorst. Before every new concentration of oxidants was examined, a fifteen-minute flow of inert argon was applied to ensure a clean system from the previously tested concentrations.

a **b**

Figure 3-5 a. Synthetic soot applied onto the monolith.
b. No remaining soot after experiment.

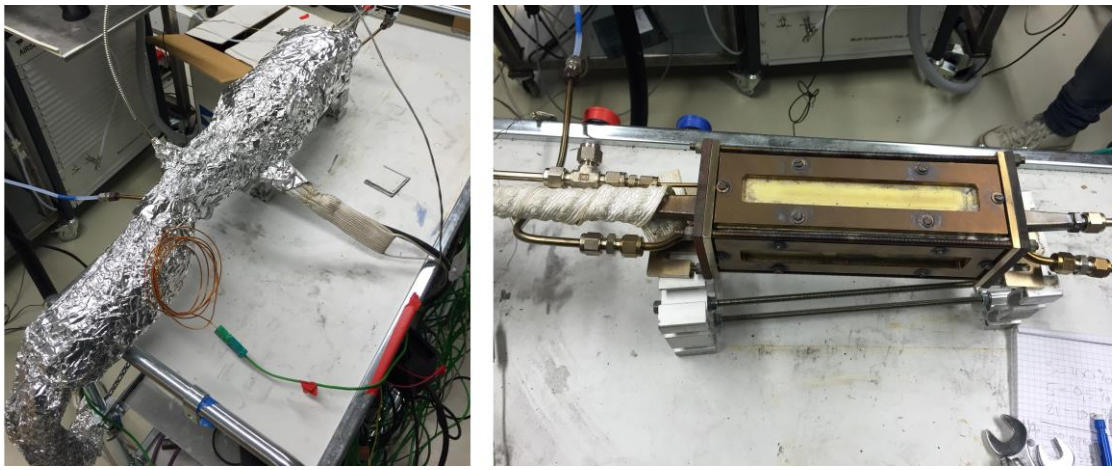

a **b**

Figure 3-6 a. Reactor insulated with glass wool and aluminum foil.
b. Reactor system assembled before insulation.

4 Simulations

This section describes how the simulations were performed and under which conditions. As mentioned earlier, the simulations aim to gain knowledge in how to perform appropriate experiments and evaluate these conditions for improving the experimental set-up.

All simulations were performed using *ANSYS Fluent 15.0* while meshing and geometry were conducted in *GAMBIT 2.4.6.*

4.1 Geometry

The geometry used for simulations were the same as for the experiments which can be noticed in Figure 3-1. However, some modifications from the existing CAD-drawing were needed to obtain a proper computational mesh. These modifications included removal of screws and associated holes. Together with this, the elongated holes for securing the reactor were removed to decrease the amount of cells used since these were not considered to affect the results of the simulation. The pipes for inserting thermocouples were also deleted for the same reason.

Since the 24 holes on each side were designed with a very small diameter (<0.75mm), a very fine mesh is needed to resolve this area of the reactor, which would be very computationally heavy. Therefore, a user defined function (UDF) was constructed to mark the position of inlet- and outlet holes and air was injected and discarded from these coordinates by the UDF. This method also allowed removal of the air pipes as well as the interior part of each side.

The simplified CAD-drawing can be seen in Figure 4-1. Pipes for thermocouples and airflow are removed. The simulations were performed in 3D. The dimensions according to Figure 4-1are:

- A: 103 mm
- B: 152.4 mm
- C: 53 mm
- D: 70 mm

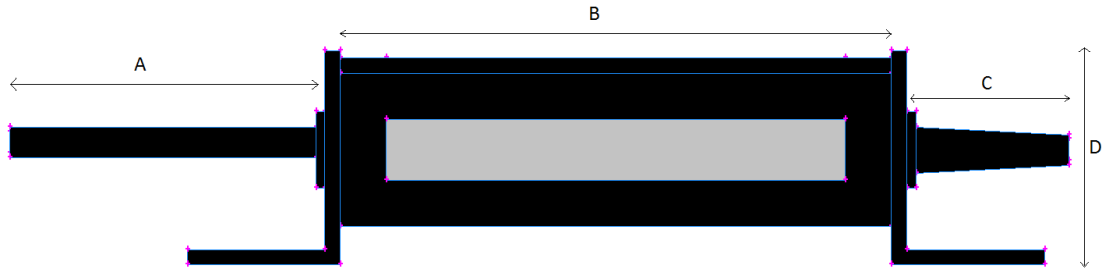

Figure 4-1 Simplified CAD-drawing.

4.2 Mesh generation

Meshing is one of the most critical and important steps in the process to generate an accurate simulation and to avoid numerical problems with convergence.

Since it is hard to evaluate the mesh before any results are obtained, a mesh was first constructed in the meshing software. This mesh was later on refined in areas of interest with large gradients in *Fluent*. In general, this procedure produces lower quality cells but the total amount of cells will be fewer and the simulations therefore less computational demanding [18]. The total amount of cells before and after adaption was approximately 1 million and 1.2 million respectively.

4.3 Simulation of hot air flow

The possibility to use a UDF as inlet- and outlet source for the air will significantly reduce the amount of cells needed for the total volume, because holes with a diameter of <0.75 mm would not be needed to be resolved. A volume and geometry of the air was created from the inlet until it enters the reactor volume through the 24 holes. The geometry was separately meshed with approximately 500 000 cells and the air flow through it was simulated. The result from this simulation gives knowledge of how the distribution of air should be described by the UDF. The volume can be seen in Figure 4-2. Same geometry was used to calculate the pressure drop of the air where the air exits the reactor volume.

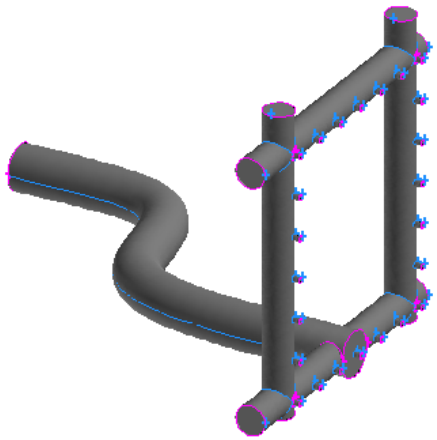

Figure 4-2 Volume of the interior air at air inlet (counter current flow).

4.4 Multiphase simulations

When simulating multiphase flow, the aim was to evaluate how the thermophoretic force affected the particles. In order do that, two different cases were simulated: one where a temperature gradient was present and one with a uniform temperature in the whole reactor volume. Comparing these two simulations gives knowledge if thermophoresis increases the number of particles migrating to the glass tube and thereby decrease the possibility to perform In-Situ experiments.

To be able to track each individual particle, Euler-Lagrange was chosen as the multiphase model and due to very small size of the particles, one-way coupling was applied since the particles were assumed not to affect the continuous phase which is reasonably due to the low Stokes number (see Appendices A). To represent real soot, size distributions of particles were applied and injections of particles were present with diameters of 20, 50, 100 and 150 nm. Important forces acting on the particles were assumed to be thermophoretic force, gravity, drag force and Brownian diffusion [11].

Due to large Knudsen number (refer Equation (2-1) and Appendices A), the drag law was corrected with the Stokes-Cunningham factor from Equation (4-1) [32].

$$C_c = 1 + \frac{2 \cdot \lambda}{D_p} \cdot (1.257 + 0.4e^{-\frac{1,1 \cdot Dp}{2 \cdot \lambda}}) \qquad \textbf{(4-1)}$$

Where λ is the mean free path of the gas, calculated from Equation (2-2) and D_p is the particle diameter. For values of C_c, refer Table A-1 in Appendices A.

During the simulations, the momentum- and energy equations were first solved to obtain a correct flow field. When the flow field was solved, particles were released from the gas inlet and tracked throughout the volume. The boundary conditions for each surface with respect to the particle are found in Table 4-1.

Table 4-1 Boundary conditions for particles on different surfaces. Reflect will perform an elastic collision while escape will store particles and enable analysis of the impinging particle properties on these surfaces.

Position	Boundary condition
Gas inlet	Injection, reflect
Walls	Reflect
Gas outlet	Outlet, escape
Monolith layer	Escape
Glass pipe walls	Escape

5 Results

In this chapter, both results from experiments and simulations are presented. While the results are presented with comments of every table and figure, a comprehensive discussion concerning the results is found in chapter *6 Discussion*.

5.1 Pressure drop

Chapter 5.1 shows the results of the pressure drop simulations. For exact geometry of the result, refer Figure 3-2 and Figure 4-2. A low pressure drop is important to minimize leakage between the gas mixture and the airflow.

5.1.1 Air inlet

Pressure drop simulations were performed over both sides of the reactor, where air enter and exits reactor volume. The result for air inlet, assuming counter current flow, can be seen in Table 5-1. The conditions where air of 400°C and atmospheric ambient pressure. For room temperature (25°C) the volumetric airflow would decrease with 57% due to density increase.

Table 5-1 Pressure drop at air inlet, holes with diameter of 0.75 mm.

Air flow [l/min]	Velocity at inlet [m/s]	Pressure drop [Pa]	Reynolds number at inlet
20	12	1505	1114
40	24	5741	2228
60	35	12092	3342
80	47	21779	4515
100	59	34373	5570
150	88	76130	8355

5.1.1.1 Air inlet, simulations and experiment

Experiments and simulations were performed to evaluate the pressure drop over the end side of the reactor, where the air enters, and assuming counter current flow. The conditions were ambient air of atmospheric pressure and airflow of 20°C with varying flow rate. The result can be seen in Figure 5-1. It can be noticed that the result from experiments and simulation agree well. From this graph, it can be concluded that further simulations of pressure drop at various conditions can be reliable.

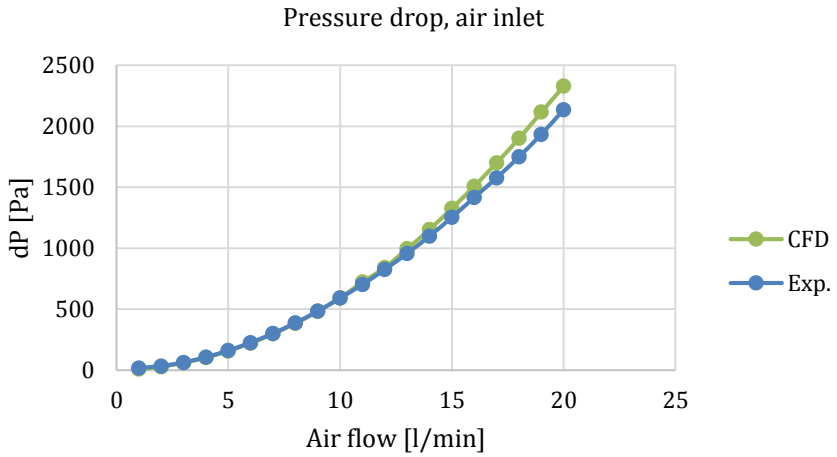

Figure 5-1 Pressure drop over air inlet (counter current flow) at 20°C, blue indicating experimental values and green simulations.

5.1.2 Air outlet

Pressure drop calculations were performed for the side of the reactor where the air exits. The result can be seen in Table 5-2. As expected the pressure drop increases with increased volumetric flow of air. The conditions were atmospheric pressure at outlet and an air temperature of 400°C. The pressure seen in Table 5-2 will be the gauge pressure in the reactor. The pressure drop over air outlet compared to the air inlet will be larger since the diameters of the holes are 0.5 mm and 0.75 mm respectively. Boundary condition of velocity inlet was applied, i.e. same velocity at all inlet holes, calculated from the total volumetric flow.

Table 5-2 Pressure drop at air outlet, holes with diameter of 0.5 mm.

Air flow [l/min]	Velocity at inlet [m/s]	Pressure drop [Pa]	Reynolds number at outlet
20	71	2281	1114
40	141	8667	2228
60	212	19067	3342
80	283	32067	4515
100	354	52159	5570
150	531	116811	8355

5.1.3 Air outlet with various hole diameters

As noticed from Table 5-2, the pressure of the air outlet side of the reactor is very large and thus the gauge pressure in the reactor. High pressure would increase the risk for air entering the gas mixture and thereby be source of error in the experiments. A larger diameter of the holes will however decrease the pressure drop. To investigate whether to increase the hole diameter or not, a study was performed for various hole diameters. The conditions for all these simulations were airflow of 400°C and a

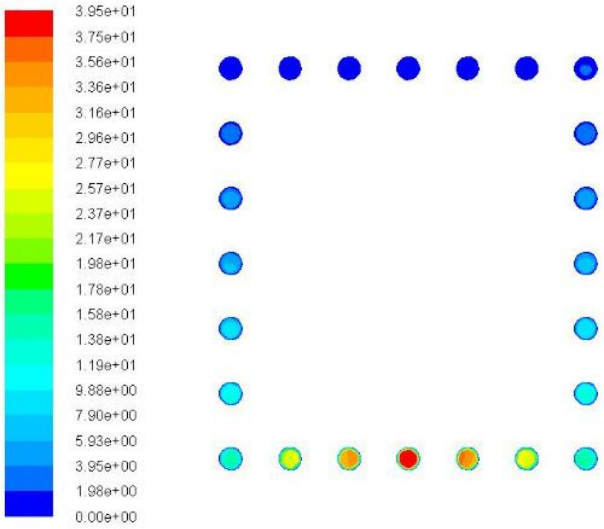

Figure 5-2 Air velocity at air outlet [m/s]. Diameter of 2 mm.

boundary condition of uniform pressure was applied. This would give knowledge about the air distribution and flow field of the air since the velocity will vary throughout the holes with larger diameter. A turbulence model of *SST k-ω* was used as well as compressible ideal gas properties since Mach numbers > 0.3 were found.

A dimensionless velocity fraction of ϕ was used for analysis, which was defined as Equation (5-1).

$$\Phi = \frac{v_{maximum} - v_{minimum}}{v_{average}} \quad \textbf{(5-1)}$$

Where the maximum velocity was assumed to occur at the lowest positioned hole, close the outlet and the minimum velocity were assumed to occur at the top, middle positioned hole. This could be verified by analyzing Figure 5-2.

Figure 5-2 shows the air velocity when the hole diameter was adjusted[1] to 2 mm. Instead of an even flow, the velocity is much greater at the middle, lowest hole than top row. This shows a variation in the velocity field, which occurs due to the increased diameter.

5.1.3.1 ϕ and pressure drop at various diameters of air outlet

Figure 5-3 is showing the pressure drop and velocity spread at various diameters at air outlet. Looking at the definition of ϕ in Equation (5-1), it can be noticed that an even flow field corresponds to a low value of ϕ since the difference of maximum- and minimum velocity are small. Tables for every individual case can be found in Appendices B. The corresponding airflow can be found in Figure 5-4.

[1] For more diameters, refer Appendices C.

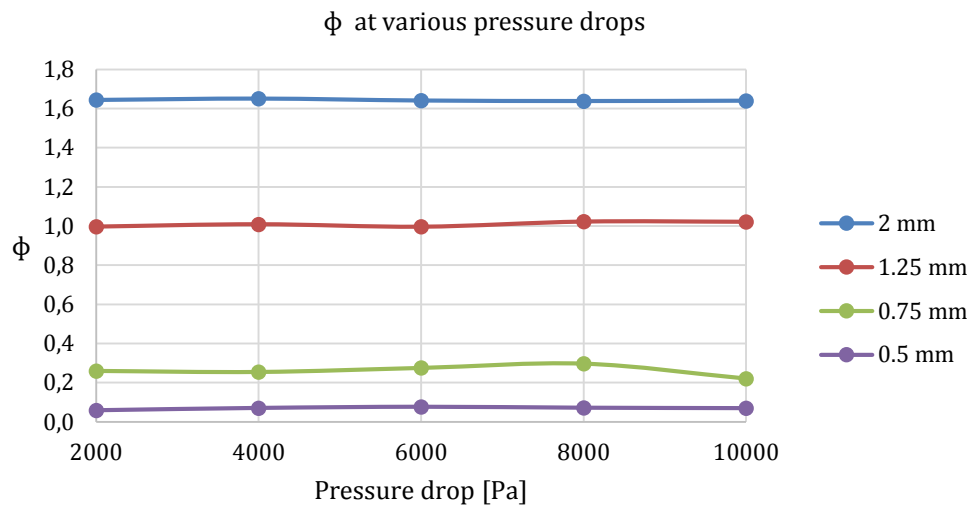

Figure 5-3 ϕ as a function of pressure drop for various diameters.

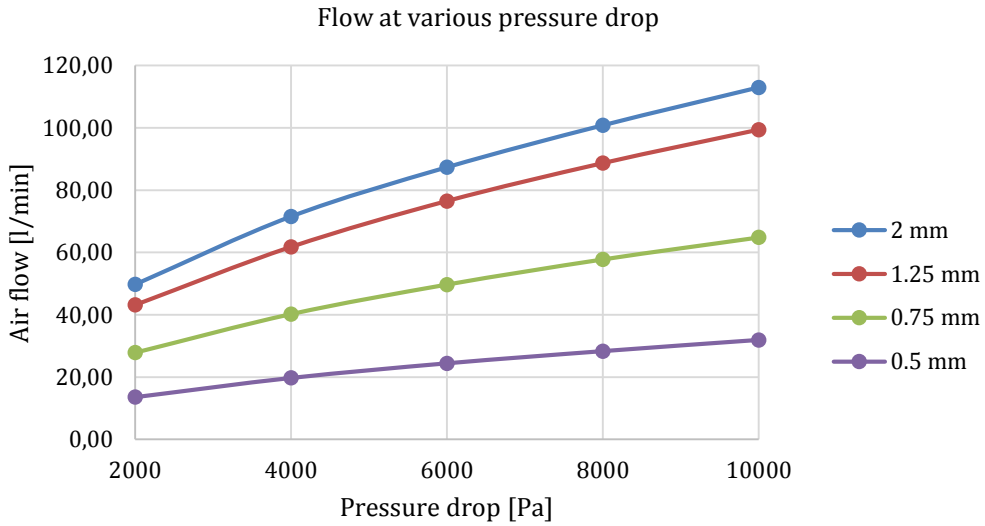

Figure 5-4 Airflow at various diameters and pressure drop.

5.2 Air distribution at air inlet

Simulations were performed to investigate the air distribution from the holes to the reactor. The result can be seen in Figure 5-5. The conditions were airflow of 20dm^3/min with a temperature of 400°C. It can be seen that the diameter of the holes are small enough to generate an even distribution of air over the total surface. The concept of using an *UDF* as inlet source for air can thereby be verified since an even distribution of the flow was obtained when solving the flow field of the air inlet.

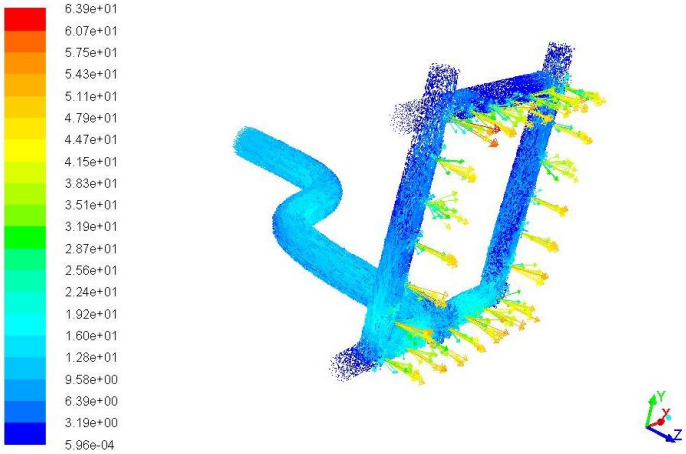

Figure 5-5 Velocity vectors from air inlet holes [m/s].

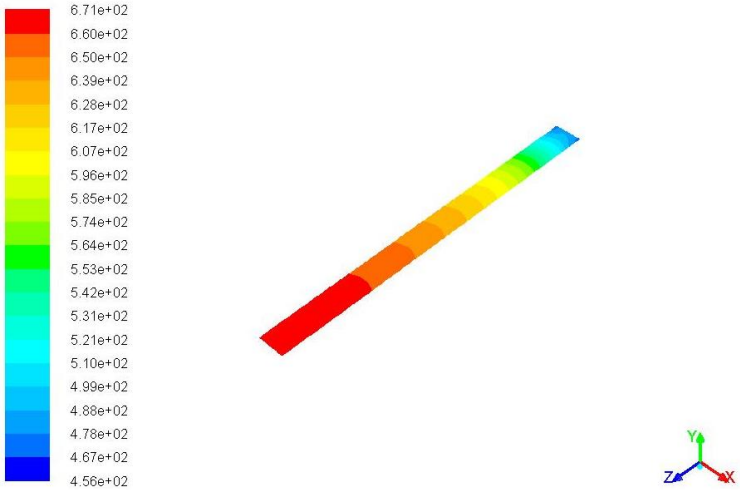

Figure 5-6 Temperature profile [K] of monolith layer, co current airflow.

5.3 Simulation of counter- and co current air flow

Simulations were conducted to investigate whether the hot isolated airflow should flow co- or counter current compared to the gas flow passing the monolith. The aim is to obtain an even distributed temperature profile over the monolith layer to ensure uniform conditions over the reaction zone i.e. the monolith. Both co- and counter current simulations were conducted with boundary conditions of an inlet pipe with a temperature of 400°C, assuming heat tape to be used for experiments and an roughly estimated heat transfer coefficient[2] of 7 $W/m^2 \cdot K$ and a free stream temperature of 25°C for other parts of reactor.

The temperature profile for co current airflow can be seen in Figure 5-6. The air flow conditions were a temperature of 400°C and a flow rate of 20 dm^3/min and exhaust gas flow of 400°C

[2] Estimated for horizontal cylinder with natural convection [23].

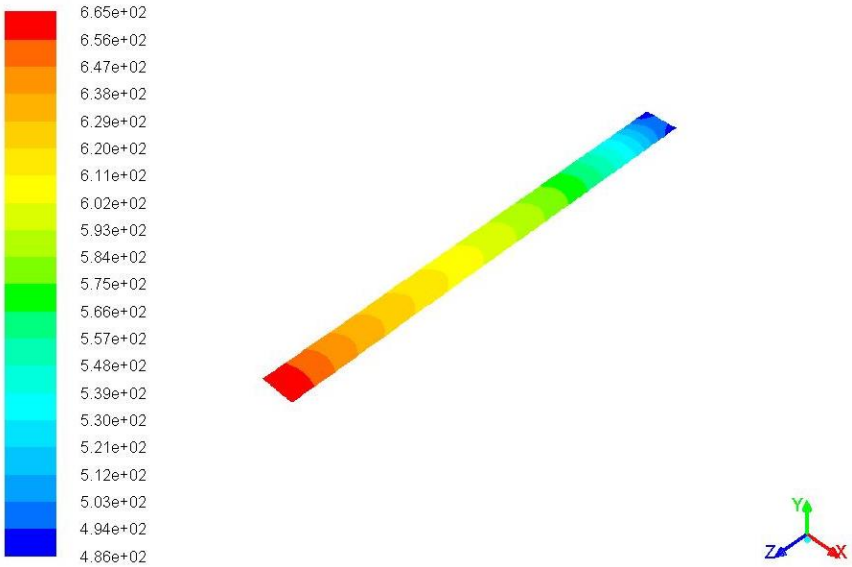

Figure 5-7 Temperature profile [K] of monolith layer, counter current airflow.

and 1 m/s. It can be noticed that highest temperature is 398°C and lowest 183°C, a temperature decrease of 215°C .

Figure 5-7 is showing the temperature profile over the monolith with counter current airflow. Boundary conditions were the same as for co current. It can be seen that the highest temperature is slightly lower, 392°C , while the lowest is 213°C , a temperature decrease of 179°C . This shows that the temperature profile is more even over the monolith layer and counter current airflow is thereby chosen for experiments. If an even higher temperature is needed, the volumetric airflow can be increased to reach higher temperatures. In addition, heat tape could be used in more areas, see Table 5-3.

5.4 Monolith temperature

Simulations were performed to analyze the temperature profile of the monolith layer. Four different cases were investigated. One were only the top window were built of quartz glass and the two side windows of stain-less steel, and one with all three windows of quartz glass. Counter current airflow was applied for all simulations. In addition to this, simulations were performed when the airflow was considered to be uneven. This scenario would appear if the outlet hole diameter would be increased.

- Case A: One glass window, even flow
- Case B: Three glass windows, even flow
- Case C: One glass window, uneven flow ($\phi > 1$, diameter of 2 mm)
- Case D: Three glass windows, uneven flow ($\phi > 1$, diameter of 2 mm)

5.4.1 Case A: Top window of glass, even flow

The temperature range over the top monolith layer was obtained for various flow rates of air. The result can be seen in Table 5-3. Conditions during simulation were a gas flow[3] of 0.26 m/s with a temperature of 400°C . Both inlet- and outlet pipes were assumed heated to 400°C with heat tape. An estimated heat transfer coefficient of 7 $W/m^2 \cdot K$ was applied to the outside of the reactor volume and accounting for radiation. The air temperature was 400°C . For this case, only the top window was assumed to be constructed of glass while both side windows were made of stainless steel.

Table 5-3 Temperature of monolith top layer, top window glass.

Air flow [l/min]	Air flow [$N \cdot dm^3/min$]	min T [°C]	max T [°C]	ΔT [°C]
20	8.70	349	397	48
40	17.39	372	398	26
60	26.09	382	398	16
80	34.79	387	399	12
100	43.48	390	399	9
150	65.22	393	399	6

5.4.2 Case B: All windows of glass, even flow

Table 5-4 is showing the temperature variation of the top monolith layer with assumption that all three windows were constructed of quartz glass. Same conditions as for Case A was applied.

Table 5-4 Temperature of monolith top layer, all windows of glass.

Air flow [l/min]	Air flow [$N \cdot dm^3/min$]	min T [°C]	max T [°C]	ΔT [°C]
20	8.70	344	397	53
40	17.39	370	398	28
60	26.09	380	398	18
80	34.79	385	399	14
100	43.48	389	399	10
150	65.22	393	399	6

[3] Gas velocity calculated to achieve same conditions as experimental set-up at *KCK* (Competence Center for Catalysis).

5.4.3 Case C: Top window of glass, uneven flow

Table 5-5 shows the temperature of the monolith layer. Only the top window constructed of glass, both side windows simulated as stainless steel. The hot air flow is simulated to be uneven and distributed as Figure 5-2.

Table 5-5 Temperature of monolith layer, top window of glass and uneven flow.

Air flow [l/min]	Air flow [N·dm^3/min]	min T [°C]	max T [°C]	ΔT [°C]
20	8.70	348	397	49
40	17.39	371	398	27
60	26.09	380	398	18
80	34.79	385	399	14
100	43.48	388	399	11
150	65.22	392	399	7

5.4.4 Case D: All windows of glass, uneven flow

Table 5-6 shows the temperature of the monolith layer. All three windows were simulated as glass and the hot air flow with an uneven distribution, same as for Case C.

As seen from Table 5.3-5.6, the monolith temperature is dependent on the volumetric flow as well as the effect of an even or uneven flow and if the windows is consisting of glass or stainless steel. The volumetric flow contributes to large extent while uneven or even flow barely makes a difference.

Table 5-6 Temperature of monolith layer, all windows of glass and uneven flow.

Air flow [l/min]	Air flow [N·dm^3/min]	min T [°C]	max T [°C]	ΔT [°C]
20	8.70	344	397	53
40	17.39	368	398	30
60	26.09	378	398	20
80	34.79	385	399	15
100	43.48	387	399	12
150	65.22	391	399	8

5.5 Heating experiments

In order the reach sufficiently high enough temperatures for reaction to occur (> 330°C), three different experimental setups were examined. Each experiment was performed with different heating equipment.

- Case I: Large heater with heating cartridge
- Case II: Air heater (700 W, max. delivery temperature of 650°C)
- Case III: Only heat tape (250 W, 500 W)

For all three cases, heat tape was used outside the reactor volume as well as on the pipe for inlet gas. The reactor was completely isolated with glass wool and aluminum foil to minimize heat losses.

Thermocouples were used in the channels of the monolith (refer Figure 3-3) as well as on the outside of the reactor and in the airflow. *Air inlet* refers to the temperature of air before the reactor and *hot airflow* to the temperature of the air inside the reactor.

5.5.1 Case I: Large heater with heating cartridge

It can be seen from Figure 5-8 that the maximum temperature reached inside the monolith is approximately 330°C. At that time, the heat tape was set on maximum effect and close to reach maximum temperature and the risk for damage was substantial. All temperatures measured inside the reactor started to level off and maximum temperature was reached. The lowest temperature was airflow inlet. Even though the capacity of the heater was high (set point 600°C), the temperature loss was large before entering the reactor. It can be noticed however, that since the air temperature inside the reactor was much larger and close to the one inside the monolith, that the high temperatures was obtained due to the heat tape and the hot airflow was actually heated by the reactor volume.

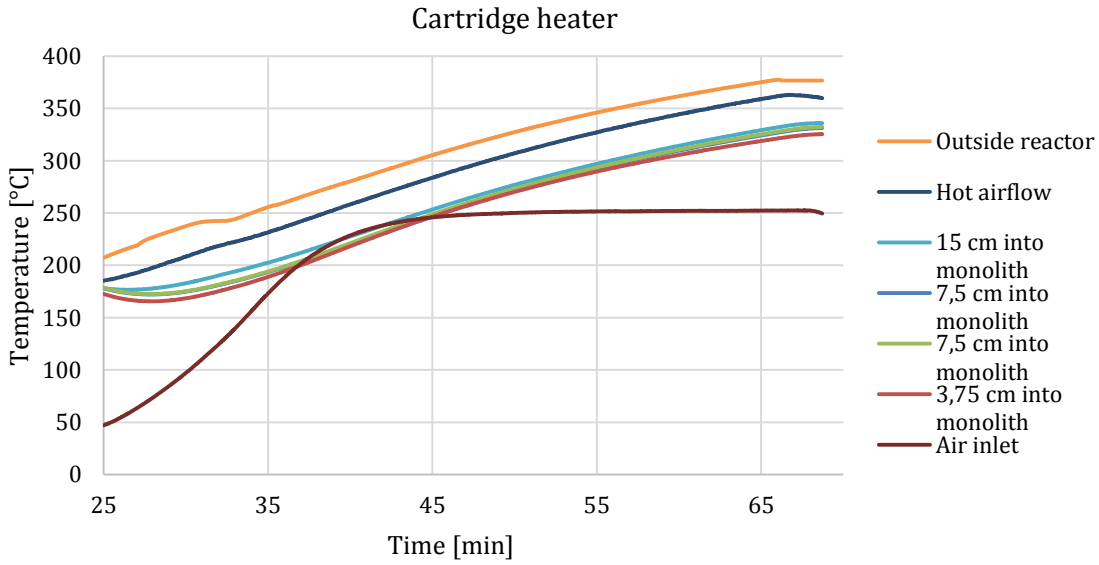

Figure 5-8 Temperatures of reactor system with cartridge heater.

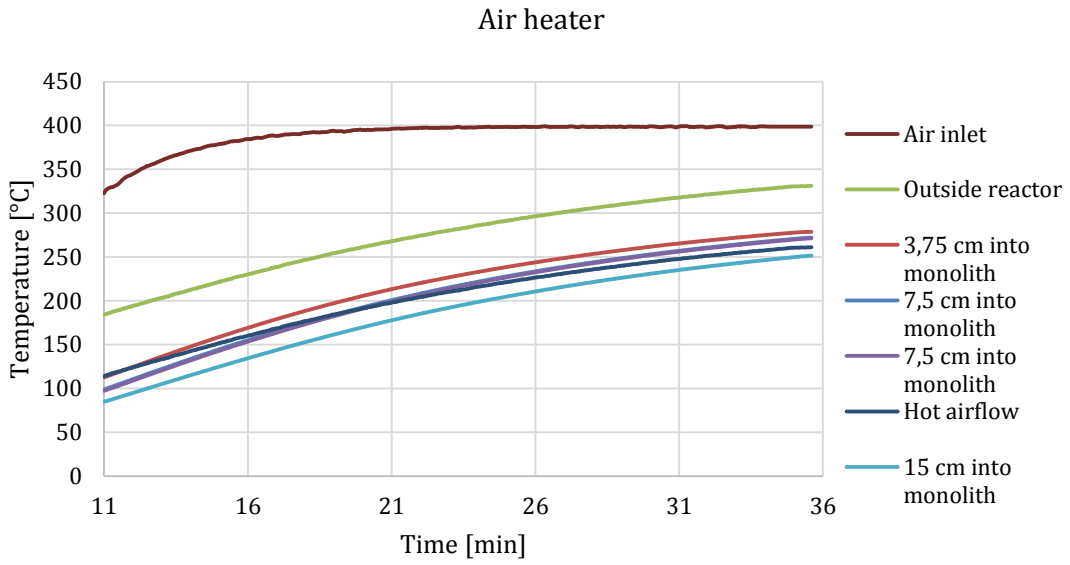

Figure 5-9 Temperatures of reactor system with air heater (Leister 15S).

5.5.2 Case II: Air heater

For the experiment with the air heater the results look similar to Case I. The result can be seen in Figure 5-9. It can be noticed however, that the losses was smaller for the air heater since the inlet temperature of air was higher compared to the cartridge heater. This originates from a more suitable experimental setup with less piping which was possible due to a more flexible position of the heater. Losses are nevertheless large since when the air was entering the reactor at 400°C, the set point of the heater was 650°C, which was the maximum power. The air heater was in addition to this, not designed for the backpressure occurring in the setup and parts of the heater were damaged. The experiment was therefore shut down.

5.5.3 Case III: Only heat tape

The result for Case I showed one very interesting effect. The hot airflow entering the reactor was actually heated by the reactor volume and therefore did not provide any heat to the system. Therefore, experiments were also performed with only gas flow. Heat tape was used at both gas inlet and the reactor volume but without any additional heater. The result can be seen in Figure 5-10. When no air was heated in the reactor, the temperature of the monolith was significantly increased. All thermocouples placed in the monolith reached temperatures larger than 380°C. Since this setup gave the highest temperature, experiments with particles were performed with this heating setup.

The temperature decrease of the thermocouple outside the reactor in Figure 5-10 after about 40 minutes occurred due to release of the safety catch of the heat tape. When this occurred, a smaller temperature gradient was applied.

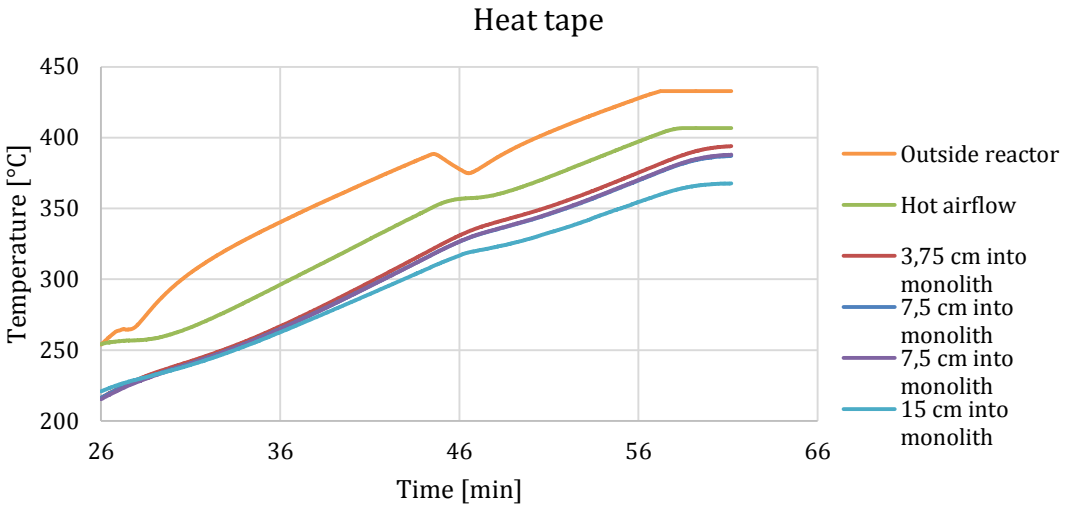

Figure 5-10 Temperatures of reactor system with heat tape only.

5.6 Simulation of NO_2 oxidation

Simulations were performed to investigate the temperature dependence on soot oxidation with NO_2 and argon as the carrier gas. According to the Arrhenius expression in Equation (2-19) the reaction rate is very sensitive to temperature. The result can be seen in Figure 5-11. A total amount of 1.1 mg soot was applied onto the monolith and NO_2 was supplied at 1500 vol. ppm, total gas flow of 330 ml/min.

The total conversion at different temperatures for ongoing oxidation in two hours is shown in Table 5-7. This result gives a good approximation of the expected time needed for experiments.

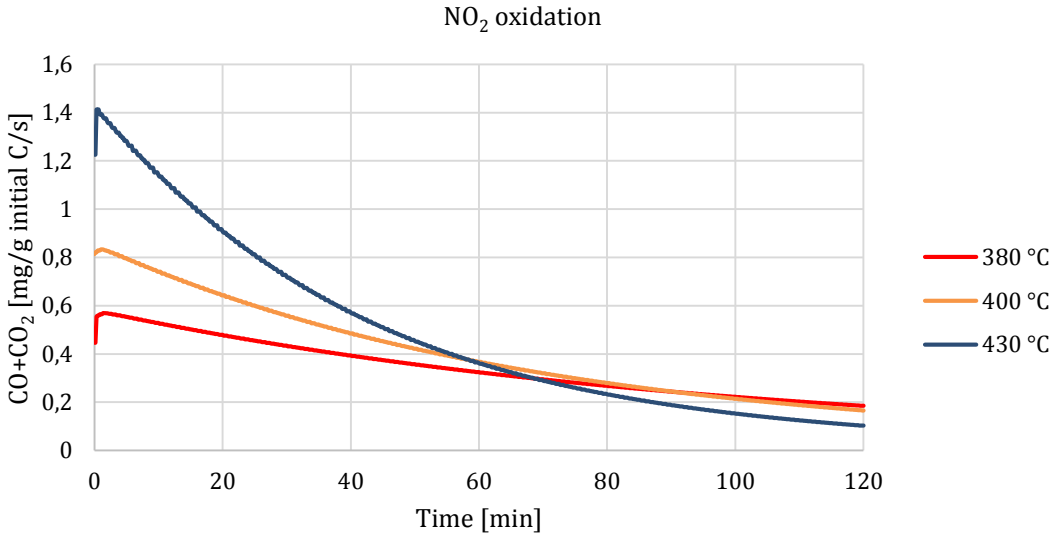

Figure 5-11 Total amount of CO and CO_2 leaving the reactor per second, normalized by the initial amount of soot.

Table 5-7 Total conversion for two hours oxidation.

Temperature [°C]	Conversion [%]
380	63.9
400	77.2
430	91.0

5.7 Soot oxidation experiment

The result of the soot oxidation experiment can be seen in Figure 5-12. On the y-axis is the concentration of CO_2 leaving the reactor in parts per million (ppm) and on the x-axis is the time for the experiment. By integrating the concentration of CO_2 with respect to time, a total amount of 92 mg Printex-U ought to have been applied onto the monolith. This value is not realistic or coherent with the measurement of the scale and is therefore discussed later on in the thesis.

Since an experiment with different concentrations and gas mixtures is reported in a single graph, an explanation can be found in Table 5-8.

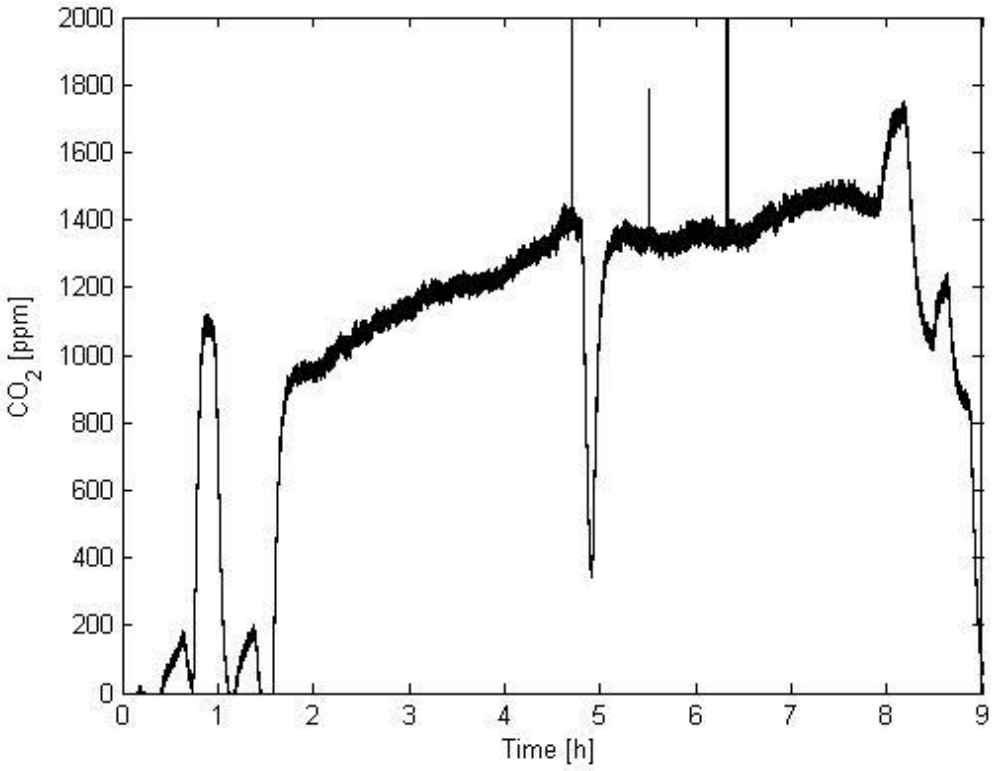

Figure 5-12 CO_2 concentration in ppm at the exhaust of the reactor system. Uniform temperature of 430°C during whole experiment and a total flow of 330 ml/min.

Table 5-8 Description of every time step, referring to Figure 5-12.

Time[h]	Gas concentration	Comment
0.5-0.8	1500 ppm NO_2	200 ppm indication of CO_2
0.8-1.1	1500 ppm NO_2 + 10 % O_2	1100 ppm indication of CO_2
1.2-1.5	1500 ppm NO_2	200 ppm indication of CO_2
1.6-4.8	1500 ppm NO_2 + 10 % O_2	1000-1400 ppm indication of CO_2. Decided to continue to with O_2 obtain complete combustion.
4.8	Inert argon	Tested if combustion still occurring. Only argon as input.
5-7.8	1500 ppm NO_2 + 10 % O_2	1400 ppm indication of CO_2 leaving the system.
7.8-8	1500 ppm NO_2 + 15 % O_2	1700 ppm indication of CO_2
8.1-8.2	1500 ppm NO_2 + 5 % O_2	1050 ppm indication of CO_2
8.2-8.4	2000 ppm NO_2 + 5 % O_2	1200 ppm indication of CO_2
8.5-8.7	1000 ppm NO_2 + 5% O_2	850 ppm indication of CO_2. Decided to quit the experiment.

5.7.1 Oxidation rate as a function of O_2 concentration

As mentioned, the presence of O_2 in the gas mixture will add a second reaction, as O_2 also will react with soot, together with NO_2. In addition to this, O_2 in excess will shift the thermodynamic equilibrium towards NO_2 (refer Figure 2-7).

With a total flow of 330 ml/min and constant concentration of 1500 ppm NO_2, the produced CO_2 as a function of O_2 is shown in Figure 5-13. Data is collected from Figure 5-12. From the figure it is clearly seen that the oxidation of soot to CO_2 is highly dependent on the concentration of O_2.

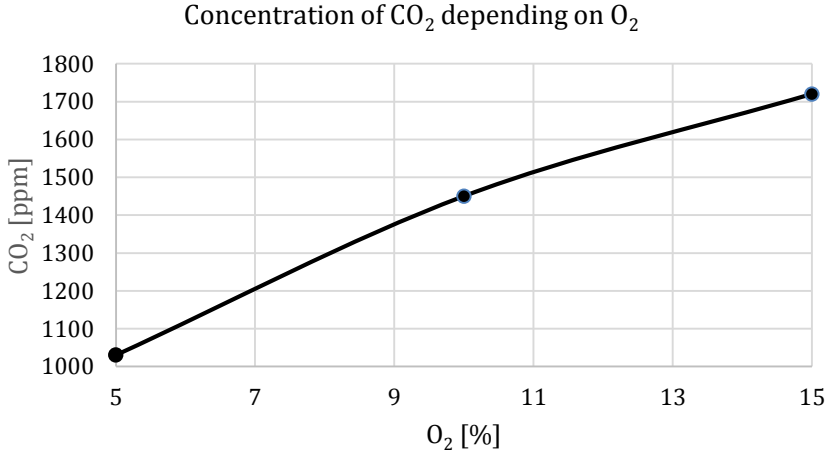

Figure 5-13 CO_2 concentration at exhaust outlet as function of O_2 concentration. During all three concentrations of O_2, the NO_2 concentration was 1500 ppm at inlet. The line is included to guide the eye.

5.8 Dispersed particles with temperature gradient

Simulations were performed to investigate were dispersed particles would end up in the reactor if the soot were not applied directly onto the monolith. For comparison, simulations were performed both with a uniform temperature of 400°C in the whole reactor volume as well as with the temperature gradient obtained when airflow of 400°C was provided without complete insulation to provide realistic conditions for In-Situ operation of the reactor. When simulated with airflow, both the monolith and glass tube is within a temperature difference of 100°C.

Table 5-9 is showing the numbers of particle captured at different positions in the reactor. It is clearly seen that the majority of the particle follow the gas flow and leave the reactor at the outlet. Due to the reactor geometry and locations with very low velocity, all particles will not leave the reactor volume in finite time.

Table 5-9 Numbers of particles captured at different positions. Hot airflow was applied to obtain temperature gradient.

D_p [nm]	Caught on glass pipe	Caught on monolith	Remaining in reactor	Outlet	Total
20	23538	2250	4543	242549	272880
50	10292	160	26915	235513	272880
100	9541	35	28815	234489	272880
150	9538	20	28773	234549	272880

Table 5-10 is showing the capture of particles in percentage, calculated from Table 5-9. The capture efficiency is decreased with increased particle diameter. As seen, the majority of the captured particles end up at the glass pipe.

Table 5-10 Percentage of particles captured at different positions in the reactor.

D_p [nm]	Capture on glass pipe [%]	Capture on monolith [%]	Total capture [%]
20	8.63	0.82	9.45
50	3.77	0.06	3.83
100	3.49	0.01	3.51
150	3.49	0.007	3.50

5.9 Dispersed particles with uniform temperature

Dispersed particles were also simulated with a uniform temperature. No airflow was supplied but instead complete isolation with no heat losses and a temperature of 400°C. Glass tube and monolith were having the same temperature over the entire domain to exclude any possible effect of thermophoresis.

Table 5-11 is showing the numbers of captured particles at different positions in the reactor while Table 5-12 is showing the percentage of captured particles at different positions, calculated from Table 5-11.

From the results it can be noticed that more particles are captured in total when a temperature gradient is present but more particles are captured by the monolith when a uniform temperature is applied.

Table 5-11 Numbers of particles captured at different positions in the reactor. Uniform temperature of 400°C.

D_p [nm]	Caught on glass pipe	Caught on monolith	Remaining in reactor	Outlet	Total
20	21284	7240	2982	241410	272880
50	8627	850	26690	236713	272880
100	8003	390	29455	235032	272880
150	8009	260	29449	235162	272880

Table 5-12 Percentage of captured particles at different positions in the reactor. Uniform temperature of 400°C.

D_p [nm]	Capture on glass pipe [%]	Capture on monolith [%]	Total capture [%]
20	7.80	2.65	10.45
50	3.16	0.31	3.47
100	2.93	0.14	3.07
150	2.93	0.09	3.02

6 Discussion

As temperature is of great importance when performing oxidation experiments, a lot of time was spent during this project to achieve a proper heating setup. Unfortunately, none of the available heaters could provide enough heat for the hot air flow to heat the monolith to a sufficient temperature. For the small flow occurring in the system, the heat losses were too large before entering the reactor volume. The results from the simulation show that either a very hot flow, and/or larger volumetric flow, is needed to obtain a small enough temperature difference over the monolith.

It was however found that using only heat tape and no airflow at all would generate a stable temperature of the monolith of above 400°C. It seems that the airflow was actually cooling down the reactor volume. This was noticed when observing the temperature of the air inlet as well as the air in the reactor, showing the result of the air in the reactor actually being warmer. As a consequence, the conclusion was that heat was removed from the reactor volume with the airflow. The downside of this set-up was that no visual access was possible.

From the soot oxidation experiment, Figure 5-12, it is easily seen that the reaction rate and oxidation of soot is much higher with the presence of O_2. The reason for this is that NO_2 is naturally degrading due to thermodynamic equilibrium to NO, a molecule that does not have the ability to oxidize soot at these temperatures. Oxygen has a stabilizing effect on NO_2 reduction (see Figure 2-7) and more NO_2 therefore has the ability to oxidize soot when O_2 is present. Figure 5-13 clearly shows a trend with oxidation rate and oxygen concentration. The higher O_2 concentration, the higher CO_2 concentration leaving the system. The same trend with NO_2 concentration was obtained.

According to Equation (2-18), there is a need of two NO_2 molecules to produce one CO_2 if the selectivity is zero, i.e. maximum production of CO_2 and zero CO. 1500 ppm NO_2 was used during the experiment and more than 1000 ppm CO_2 was produced during the experiment which also indicates that O_2 is reacting according to Equation (2-22), even at as low temperature as 430°C.

It is of utmost importance that the combustion is complete to determine the exact amount of synthetic soot applied onto the monolith. According to the simulations, this should not take much longer than two hours. For that reason, the main part of the experiment was performed with the presence of O_2 to increase the oxidation rate. It is however very unlikely that the soot was not completely oxidized after nine hours. Consequently the experiment was stopped and analyzed. Integration of the total amount CO_2 leaving the system with time showed that 92 mg Printex-U had to have been applied onto the monolith, an unrealistic amount when comparing to the scale measurements before the experiment was conducted. This indicates that something else also had reacted during formation of CO_2. To seal the reactor and avoid leakage of gas, a graphite gasket was used. Unfortunately, it is most likely that the carbon atoms in the gasket were reacting with the gas with the effect of producing CO_2. This would explain the large amount of produced CO_2, a still ongoing process when it was decided to shut down the experiment. Even if it is possible that some particles were still present on the monolith, hidden in the pores, there were no particles left visible to the naked eye.

The reaction rate of soot oxidation is dependent on the amount of soot: the more soot present, the higher the reaction rate. This reasoning would with a perfectly conducted experiment produce a graph of decreasing CO_2 production with time as shown by simulation in Figure 5-11. This means that the reaction rate should be highest at the first period with combination of NO_2 and O_2. It can be seen from Figure 5-12 that the CO_2 concentration at this time was about 1100 ppm. Starting next cycle with NO_2 and O_2 generates a CO_2 concentration of just below 1000 ppm but, unrealistically, increasing with time. This might indicate that the soot combustion was complete after about 2 hours and later on the gasket started to oxidize, generating higher CO_2 at outlet than in the beginning of the experiment. No type of graphite gasket should for future experiments be used when performing soot oxidation.

When simulating a dispersed flow of particles in the reactor the Reynolds number was evaluated to 35 based on the hydraulic diameter, i.e. laminar flow. As the Stokes number was well below unity, the particles were following the fluid streamlines well and due to the Reynolds number, no turbulent dispersion was present. This means that the particles only have the possibility to escape or leave the streamlines and reach the walls by thermophoresis and Brownian motion. Due to the very small size of the particles, gravity does not affect the motion of the particles significantly [33]. Particles of varying size were simulated to obtain knowledge in how different particles behave due to different forces.

From the multiphase results in chapter 5.8-5.9, it is clearly seen that the majority of particles is following the streamlines well and leave the reactor by the exhaust gas at the outlet. This result is independent of the boundary conditions of the temperature, uniform or with a gradient. It is also seen that the smallest particles, 20 nm, is the size that reaches the glass tube and monolith to largest extent. This result originates from the Brownian motion, which is most pronounced for the smallest of particles. This random motion enables particles to deviate from the fluid streamlines and thereby reach the boundaries of the glass tube and monolith.

When uniform temperature was applied, the total capture was about the same as for the case with a gradient. The distribution between the glass tube and the monolith differed in that more particles were captured by the monolith, which indicates a very small but yet an effect of thermophoresis for the case with a temperature gradient. The main reason for more particles reaching the glass tube than the monolith is however the available area. The area of the glass tube is twice that of the monolith top layer.

In order to perform experiments with a particle dispenser, more particles need to reach the monolith. Only particles reaching this area have the time to oxidize. A decreased velocity or larger monolith, completely filling the glass tube, could work when performing experiments with this setup.

Several simulations have been performed during this project to gain knowledge about the In-Situ reactor and the system around it. The pressure drop of different flows has been calculated and the reactor has been modified in various ways to perform better. Based on the results of these simulations, the holes for the existing air flow have been drilled to increase the diameter and thereby lower the built-up pressure in the reactor,

some parts of the reactor have been reinforced to manage the tension that the reactor is exposed to, etc.

All simulations provide good information of how the reactor can perform in the ideal case. This includes temperature of needed airflow, size of the flow, co- or counter airflow among others. The problems still needing to be solved is now more of a practical character. Assuming air heaters will be used in the future, the temperature actually entering the reactor must be high enough to stabilize the monolith temperature without insulation and heat tape blocking the windows to ensure In-Situ operation. This also requires a more proper gasket to minimize leakage and thereby heat losses, especially eliminating the risk of oxidants reacting with unwanted compounds. Some modification is also needed around the windows of the designed reactor. As designed now, there is no space for a soft gasket above or below the windows. And when experiments were performed, the buildup tension in the reactor ruptured all parts of glass.

7 Conclusions

In this thesis, an iterative method has been applied to gain knowledge in the soot oxidation process from diesel vehicles and characterize the behavior of a newly designed in-situ reactor. Experiments and CFD simulations have been used together to get deeper understanding of the processes occurring.

Based on CFD simulations, experiments have been performed to validate the results and try to implement them in a practical manner. The CFD simulations have gained increased understanding of the design and the subsequent behavior of the reactor. Potential problems related to heating and of soot oxidation in the reactor have been identified and solutions have been proposed. Modifications of the reactor have been carried out due to simulations and experiments to obtain a better setup for the reactor system. Some of the modifications include reinforcement of the reactor as well as increasing of diameters for the airflow to not obtain a too large gauge pressure in the reactor.

Multiphase CFD simulations have also been conducted to gain knowledge in the distribution of the particles in the reactor. The results show that a particle dispenser can be used for experiments but more effectively with a larger monolith that uses all channels and thereby not to be performed with In-Situ operations. The effect of thermophoresis is small and the result of the multiphase simulations shows that the majority of the particles is leaving the reactor with the gas flow.

8 Future work

Since the usage of vehicles is still increasing, the need to further improve the EATS is of great importance. Emissions still pollutes our cities to a high degree. Research within this area is still of great importance and the industry is constantly using new ideas and breakthroughs for developing new filters. With our project, we hope to have made a small contribution to the field and inspired or motivated more people to join the research area.

Regarding our project and the designed reactor, there is still work to be done. The idea and intention with the reactor, to use it In-Situ, with glass windows and actually look at the oxidation is a fantastic idea and have potential to increase the knowledge within particle oxidation to a great extent. There are however obstacles to overcome, especially regarding heating to obtain the high temperatures needed for soot oxidation. Generating that high temperature and keeping it constant without insulation or blocking the windows is a problem yet so solve. Luckily, this is already a project that involving more people to carry on our work and hopefully a solution will present in a near future. We can't wait to see the result.

9 References

1. Organization, W.H., *Health aspects of air pollution with particulate matter, ozone and nitrogen dioxide: Report on a WHO Working Group*. 2003: World Health Organization, WHO, Regional Office for Europe.
2. Agency, E.E., *Transport and environment: on the way to a new common transport policy*. 2007, European Environmental Agency: Copenhagen, Denmark.
3. Agency, U.E.P., *Health assessment document for diesel engine exhaust*. 2002, National Centre for Environmental Assessment Washington^ eDC DC.
4. Kittelson, D.B., *Engines and nanoparticles: a review.* Journal of Aerosol Science, 1998. **29**(5–6): p. 575-588.
5. Johnson, J.H., et al., *A Review of Diesel Particulate Control Technology and Emissions Effects - 1992 Horning Memorial Award Lecture*. 1994, SAE International.
6. Organization, W.H., *HEALTH EFFECTS OF PARTICULATE MATTER*, ed. W.H. Organization. 2013, Copenhagen, Denmark.
7. C.Hinds, W., *Aerosol Technology PROPERTIES, BEHAVIOR, AND MEASUREMENT OF AIRBORNE PARTICLES*. Second ed. 1999: WILEY-INTERSCIENCE.
8. Silva, R.A., et al., *Global premature mortality due to anthropogenic outdoor air pollution and the contribution of past climate change.* Environmental Research Letters, 2013. **8**(3): p. 034005.
9. Konstandopoulos, A.G. and E. Papaioannou, *Update on the science and technology of diesel particulate filters.* KONA Powder and Particle Journal, 2008. **26**(0): p. 36-65.
10. Xin, Q., *1 - The analytical design process and diesel engine system design*, in *Diesel Engine System Design*, Q. Xin, Editor. 2013, Woodhead Publishing. p. 3-112.
11. Ström, H., *Particulate Flows in Aftertreatment Systems*, in *Department of Chemical and Biological Engineering*. 2011, Chalmers University of Technology: Göteborg, Sweden.
12. Farrauto, R.J. and K.E. Voss, *Monolithic diesel oxidation catalysts.* Applied Catalysis B: Environmental, 1996. **10**(1–3): p. 29-51.
13. Kandylas, I.P. and G.C. Koltsakis, *NO2-assisted regeneration of diesel particulate filters: a modeling study.* Industrial & engineering chemistry research, 2002. **41**(9): p. 2115-2123.
14. Adler, J., *Ceramic Diesel Particulate Filters.* International Journal of Applied Ceramic Technology, 2005. **2**(6): p. 429-439.
15. Koebel, M., M. Elsener, and M. Kleemann, *Urea-SCR: a promising technique to reduce NOx emissions from automotive diesel engines.* Catalysis today, 2000. **59**(3): p. 335-345.
16. Cercignani, C., *Rarefied gas dynamics: from basic concepts to actual calculations*. Vol. 21. 2000: Cambridge University Press.
17. Crowe, C.T., et al., *MULTIPHASE FLOWS with DROPLETS and PARTICLES*. Vol. SECOND EDITION. 2012: CRC Press.
18. Andersson, B., et al., *Computational Fluid Dynamics for Engineers*. 10th edition ed. 2014.

19. Maxwell, J.C., *II. Illustrations of the dynamical theory of gases.* The London, Edinburgh, and Dublin Philosophical Magazine and Journal of Science, 1860. **20**(130): p. 21-37.
20. White, F.M., *Fluid Mechanics*. Second ed. 1987, Singapore: McGraw-Hill Book Company.
21. Stokes, G.G., *On the effect of the internal friction of fluids on the motion of pendulums*. Vol. 9. 1851: Pitt Press.
22. Maxey, M.R. and J.J. Riley, *Equation of motion for a small rigid sphere in a nonuniform flow.* Physics of Fluids (1958-1988), 1983. **26**(4): p. 883-889.
23. Welty, J.R., et al., *Fundamentals of momentum, heat, and mass transfer*. 2009: John Wiley & Sons.
24. Lapple, C. and C. Shepherd, *Calculation of particle trajectories.* Industrial & Engineering Chemistry, 1940. **32**(5): p. 605-617.
25. Jean, R.-H. and L.-S. Fan, *On the model equations of Gibilaro and Foscolo with corrected buoyancy force.* Powder technology, 1992. **72**(3): p. 201-205.
26. Talbot, L., et al., *Thermophoresis of particles in a heated boundary layer.* Journal of Fluid Mechanics, 1980. **101**(04): p. 737-758.
27. Loyalka, S., *Thermophoretic force on a single particle—I. Numerical solution of the linearized Boltzmann equation.* Journal of aerosol science, 1992. **23**(3): p. 291-300.
28. Alvarez, H., *ENERGI TEKNIK*. 3:3 ed. Vol. 1. 2008, Beijing: Studentlitteratur.
29. Wang-Hansen, C., S. Soltani, and B. Andersson, *Kinetic analysis of O2-and NO2-based oxidation of synthetic soot.* The Journal of Physical Chemistry C, 2012. **117**(1): p. 522-531.
30. Huffman, R.E. and N. Davidson, *Shock Waves in Chemical Kinetics: The Thermal Decomposition of NO21a.* Journal of the American Chemical Society, 1959. **81**(10): p. 2311-2316.
31. Laidler, K.J., *The development of the Arrhenius equation.* Journal of Chemical Education, 1984. **61**(6): p. 494.
32. Ansys Inc. *ANSYS Fluent Theory Guide*, Release 15.0, November 2013
33. Ström, H., Sasic, S., & Andersson, B. (2010). Design of automotive flow-through catalysts with optimized soot trapping capability. *Chemical Engineering Journal*, **165**(3), 934-945.

Appendices

A: Dimensionless numbers and multiphase analysis

According to Equation (2-8), the particle Reynolds number is evaluated. The values considered are estimated at 400°C and atmospheric pressure for air being the continuous phase.

$\mu_c = 3.29 \cdot 10^{-5}$ [Pa·s]

$\rho_c = 0.517$ [kg/m^3]

$D_p = 150 \cdot 10^{-9}$ [m], largest used particles

$u_c - u_d = 0.26$ [m/s], Velocity chosen to obtain a proper flow for the mass spectrometer.

$$Re_p = \frac{0.517 \cdot 150 \cdot 10^{-9} \cdot 0.26}{3.29 \cdot 10^{-5}} = 0.000612 \ll 1$$

This calculation shows that the flow can be considered to be in the *Stokes regime*. Due to the low Re_p, Equation (2-7) can be simplified and calculated as below:

$\rho_d = 1000$ [kg/m^3], mean value for Printex-U

$$\tau_{xp} = \frac{1000 \cdot (50 \cdot 10^{-9})^2 \cdot 5.47}{18 \cdot 3.29 \cdot 10^{-5}} = 2.3 \cdot 10^{-8} s$$

From this, the Stokes number from Equation (2-7) can be evaluated with a characteristic time scale of the flow calculated with the gas velocity and characteristic length of an obstacle.

$$St = 2.3 \cdot 10^{-8} s \cdot \frac{0.26}{0.0014} = 4.27 \cdot 10^{-6} \ll 1$$

The low Stokes number indicates that the inertia of the particles is very low and the particles will follow the fluid streamline very well.

Evaluating the Knudsen number from Equation (2-1) for the largest dispersed particles and the mean free path from Equation (2-2):

$$\lambda = \frac{42.2 \cdot 10^{-6}}{0.449 \cdot 0.714 \sqrt{\frac{8 \cdot 101325}{\pi \cdot 0.714}}} = 219\, nm$$

$$Kn = \frac{219}{150} = 1.46$$

As this value is greater than 10^{-3}, that would be the case for all particles since 150 nm is the largest diameter of the dispersed particles.

Since $Kn > 10^{-3}$, the drag law is corrected with the Stokes-Cunningham factor. Calculated Cunningham factors for 400°C, C_c are shown in Table A-1

Table A-1 Cunningham correction factors for different particle diameters.

Particle diameter [nm]	C_c
20	36.86
50	15.10
100	7.87
150	5.47

B: Data for calculation of ϕ

Table B-1 Data for 0.5 mm.

$v_{maximum}$	$v_{minimum}$	$v_{average}$	ϕ	Pressure drop [Pa]	Airflow [l/min]	Re (v_{max})	Re (v_{min})	Re (channel)
50.11	47.25	48.61	0.059	2000	13.59	395	372	543
73.03	68.09	69.92	0.071	4000	19.74	575	536	789
90.05	83.47	85.90	0.077	6000	24.42	709	657	976
103.34	96.23	99.06	0.072	8000	28.32	814	758	1132
115.11	107.42	110.57	0.070	10000	31.91	906	846	1276

Table B-1 shows the data for air outlet holes of diameter 0.5 mm.

Table B-2 Data for 0.75 mm.

$v_{maximum}$	$v_{minimum}$	$v_{average}$	ϕ	Pressure drop [Pa]	Airflow [l/min]	Re (v_{max})	Re (v_{min})	Re (channel)
50.90	39.34	44.44	0.260	2000	27.85	601	465	1107
72.27	56.24	62.88	0.55	4000	40.22	854	664	1600
90.56	69.15	77.73	0.275	6000	49.70	1070	817	1976
106.29	79.68	89.46	0.297	8000	57.77	1255	941	2296
110.30	88.33	99.41	0.221	10000	64.82	1303	1043	2586

Table B-2 shows the data for air outlet holes of diameter 0.75 mm.

Table B-3 Data for 1.25 mm.

$v_{maximum}$	$v_{minimum}$	$v_{average}$	ϕ	Pressure drop [Pa]	Airflow [l/min]	Re (v_{max})	Re (v_{min})	Re (channel)
42.04	13.81	28.33	0.997	2000	43.14	826	272	1673
59.97	19.63	39.99	1.009	4000	61.79	1181	386	2397
72.32	23.90	48.61	0.996	6000	76.52	1424	470	2974
84.25	27.54	55.47	1.022	8000	88.68	1658	542	3446
93.23	30.65	61.27	1.021	10000	99.43	1835	603	3867

Table B-3 shows the data for air outlet holes of diameter 1.25 mm.

Table B-4 Data for 2 mm.

$v_{maximum}$	$v_{minimum}$	$v_{average}$	ϕ	Pressure drop [Pa]	Airflow [l/min]	Re (v_{max})	Re (v_{min})	Re (channel)
39.18	1.17	23.12	1.644	2000	49.72	1234	37	1768
54.81	1.69	32.18	1.651	4000	71.52	1726	53	2556
66.34	2.06	39.17	1.614	6000	87.33	2089	64	3125
75.45	2.46	45.50	1.638	8000	100.79	2376	77	3616
83.71	2.64	49.43	1.64	10000	112.95	2637	83	4059

Table B-4 shows the data for air outlet holes of diameter 2.0 mm.

C: Velocity distribution at air outlet

Figure C.1-C.4 shows the velocity at air outlet holes. In all figures, the pressure drop is 2000 Pa.

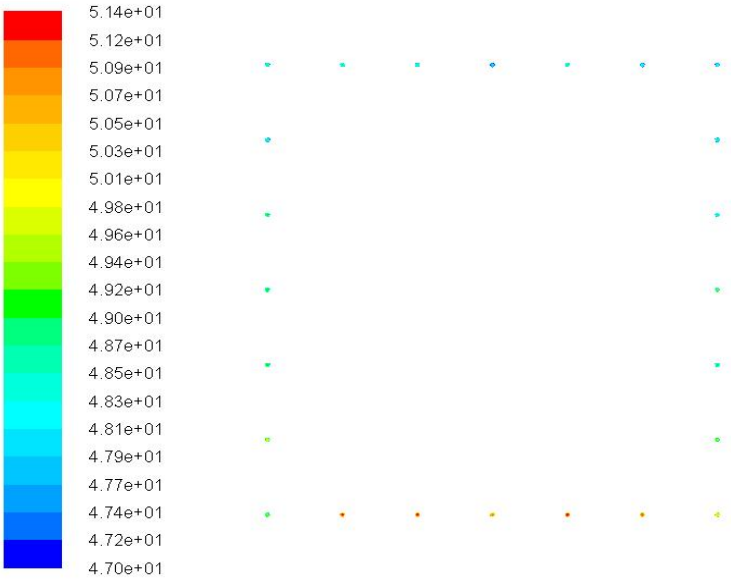

Figure C-1 Velocity at air outlet. Diameter of 0.5 mm.

Figure C-1 shows the velocity of air at air outlet with diameter of 0.5mm. It can be noticed that the velocity is approximately uniform, only differing 4 m/s from maximum to minimum velocity. For Figure C-1, ϕ according to Equation (5-1) is 0.1.

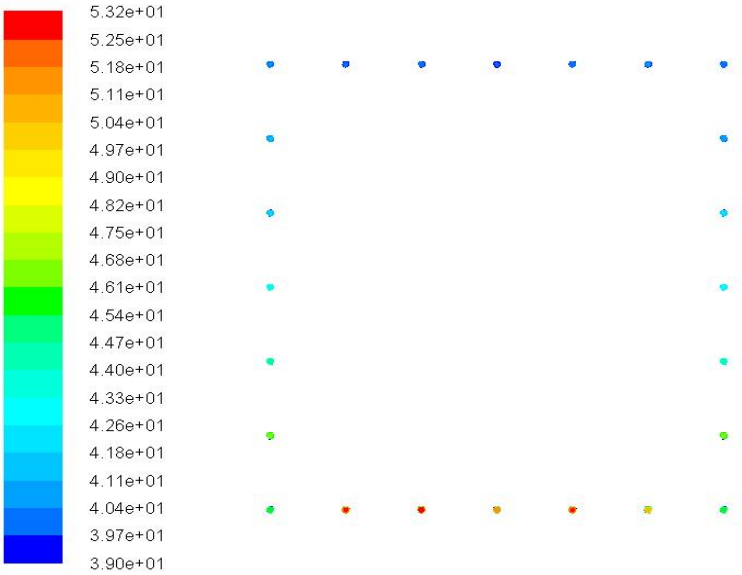

Figure C-2 Velocity at air outlet. Diameter of 0.75 mm.

Figure C-2 shows the velocity at air outlet with diameter of 0.75 mm. From the figure it can be seen that the maximum and minimum velocity differs by 14 m/s. For Figure C-2, ϕ according to Equation (5-1) is approximately 0.25.

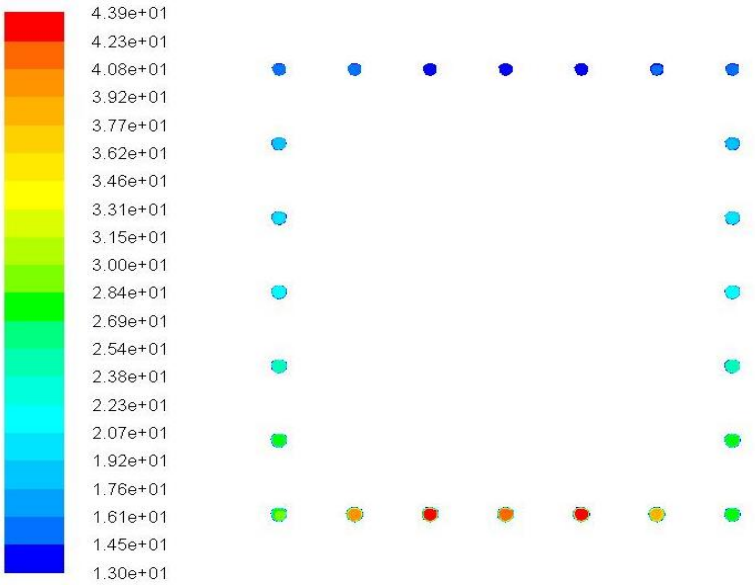

Figure C-3 Velocity at air outlet. Diameter of 1.25 mm.

Figure C-3 shows the velocity at air outlet with diameter of 1.25 mm. The difference between maximum and minimum velocity is 31 m/s and the flow is therefore considered to be clearly uneven. For Figure C-3, ϕ according to Equation (5-1) is approximately 1.

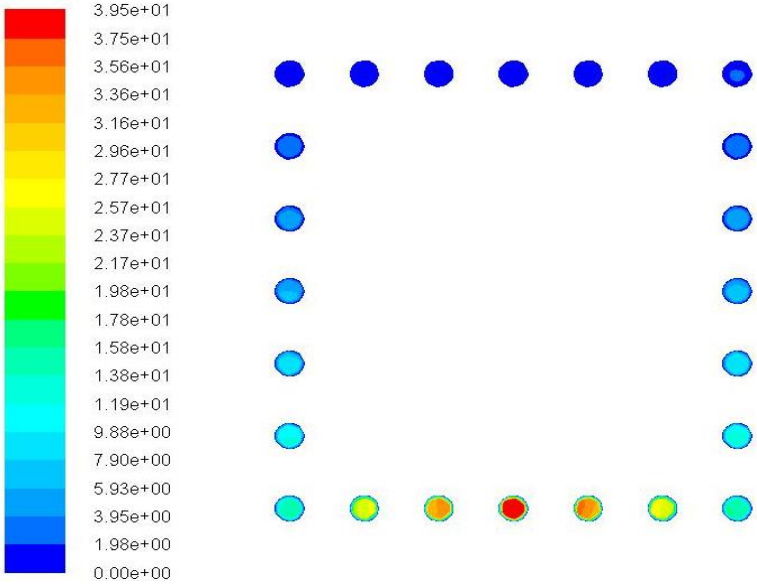

Figure C-4 Velocity at air outlet. Diameter of 2 mm.

Figure C-4 shows the velocity of air at outlet with diameter of 2 mm. The maximum velocity is almost 40 m/s while the minimum velocity is just above zero and the flow considered being uneven. For Figure C-4, ϕ according to Equation (5-1) is 1.65.

D: Kinetic data

Data for the calculation of the rate expression in Equation (2-20) with the Arrhenius equation in (2-19) are found in Table D-1.

Table D-1 Data for kinetics implemented in UDF-model.

Reaction species	k [-] (T_{ref})	E_a [kJ/mol]	β
NO_2	394.7e-6	75.4	0.89

E: Assessing convergence

Assessment of the convergence in the CFD simulations has been performed in several ways. Analyzing the local mass imbalance, monitoring of residuals as well as improving the mesh during simulations. For example, the total number of cells was increased by 20% when solving for the monolith temperature. The increase in cell number changed the temperature difference less than 0.4°C.

When simulating the motion of the dispersed particles, it is of great importance that the particles are even distributed at the inlet. Several different injections with different amount of particles have been evaluated. The generated solutions provide a result with the same capturing of particles (by percentage) both at monolith and glass tube, which also indicates an accurate solution.

F: Velocity vectors for large Φ value

Figure F-1 shows the velocity vectors for new design when the outlet diameter is changed to 2 mm. As can be seen, the velocity is largest at the bottom and a larger volumetric airflow is leaving the reactor as this area.

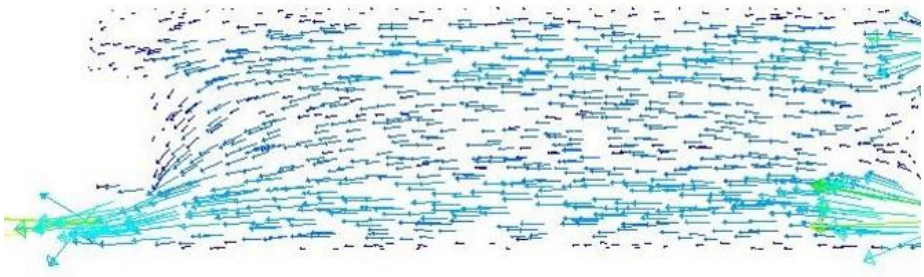

Figure F-1 Velocity vectors for diameter increase to 2 mm, Φ value of 1.64.